University of Stavanger

FACULTY OF SCIENCE AND TECHNOLOGY

MASTER'S THESIS

Study program/specialization: MSc in Offshore Technology / Marine and Subsea Technology	Spring/Autumn semester, 2019 Open
Writer: Vadim Yu	*(signature)* (Writer's signature)
Faculty supervisor: Professor Ove Tobias Gudmestad External supervisor: Professor Anatoly Borisovich Zolotukhin	
Title of master's thesis: Concept of a Pipeline Protection against Ice Ridges and Vortex-Induced Vibrations	
Credits (ECTS): 30	
Keywords: Sakhalin, ice ridge, ice gouging, vortex shedding, turbulent flow, CFD, OpenFOAM, URANS	Number of pages: 76 + supplemental material/other: 3 Stavanger, June 10, 2019

ABSTRACT

The development of offshore oil and gas fields involves a few challenges concerning the pipeline on-bottom protection, particularly in the Arctic zone. In the shallow waters the ice ridges may make dangerous gouges, hence, damaging pipelines. In the deep waters when a pipeline has free spans, it is subjected to vortex-induced vibrations (VIV). This thesis is focused in these challenges having in mind that other aspects like damages due to falling objects, trawling and interaction with anchors also are of concern for a full study of the protection of pipelines.

The research is provided by the example of the Sakhalin offshore. It is considered to be a sub-arctic zone which includes a few important oil and gas fields.

The thesis describes the *pipeline interaction with the first-year ice ridges*. A study of probable sizes, mechanical properties and geometrical parameters of the ridges is performed in order to calculate the ice scouring depth.

Further, in order to analyze *the motion of cylindrical structures undergoing VIV* numerical simulations are used as an example. In the numerical simulations, the behavior of the near-bottom VIV of a single cylinder and two closely spaced cylinders is investigated at high Reynolds number. The study is performed using the computational fluid dynamics code OpenFOAM. 2D models are simulated at a Reynolds number, $Re = 3.6 \times 10^6$, gap ratio $e/D = 1$ and 2 for the single cylinder and the two cylinders, respectively, and at range of distance between cylinders $L = 4D$ to $6D$. These values are considered realistic for tandem on-bottom pipelines.

In both the ice ridge and the VIV cases the *protection of the pipeline* may be required. The protection of a pipeline due to ice scouring is investigated by means of trench construction. To investigate the effect of reducing the effect of VIV, the elimination of free spans due to rock dumping is considered. Finally, a discussion of the environmental impact of trenching a pipeline or rock dumping is given.

ACKNOWLEDGMENTS

I would like to thank my supervisors Prof. Ove Tobias Gudmestad and Prof. Analoty Borisovich Zolotukhin for giving me the possibility to work under their supervision during writing my Master's thesis. Thank you for your consulting, both technical and mental support and coordination. You gave me the opportunity to develop my interest in Arctic technologies.

Moreover, I would like to express the appreciation to Prof. Muk Chen Ong and Marek Jan Janocha for their constructive discussions and support in Computational Fluid Dynamics. You have opened for me the new field of science and excited my interest in CFD modelling, thank you.

I am also appreciated to University of Stavanger for providing the necessary technical resources necessary to finish the master's thesis.

In closing, I would like to thank my parents, my family for their support and aid.

CONTENTS

LIST OF FIGURES

LIST OF TABLES

ACRONYMS

BD	Burial Depth
CFD	Computational Fluid Dynamics
CSD	Cutter Suction Dredger
DoF	Degree of Freedom
FFT	Fast Fourier Transform
FIM	Flow-Induced Motion
RMS	Root-Mean-Square
ROV	Remotely Operated Vehicle
SST	Shear Stress Transport
TSHD	Trailing Suction Hopper Dredger
URANS	Unsteady Reynolds-Averaged Navier-Stokes
VIV	Vortex-Induced Vibrations

SYMBOLS

ROMAN SYMBOLS

A_c	Current projected area
A_{w1}	Wind projected area
A_{w2}	Wind projected area (skin effect)
a	Amplitude
B	Ridge breadth
C_D	Drag coefficient
C_{dc}	Current drag coefficient
C_{dw}	Wind drag coefficient
C_L	Lift coefficient
C_{sw}	Wind skin coefficient
D	Diameter
D_{pipe}	Outer diameter of a pipe
d	Gouge depth
E	Elasticity modulus
E_i	Ice field potential energy
E_k	Ridge kinetic energy
E_p	Ridge potential energy
e	Gap height
F_b	Buoyancy force
F_C	Coulomb's friction force
F_D	Drag force
F_{dc}	Drag force from current
F_{dw}	Drag force from wind
F_L	Lift force
F_f	Friction force / force from surrounding floe
F_{fr}	Friction force of the ice ridge
F_p	Pressure force
F_t	Tension force of the ice field
f_n	Natural frequency
f_{osc}	Oscillation frequency
f_{st}	Strouhal frequency
h	Level ice thickness

h_1	Frontal mound
h_c	Consolidated layer thickness
h_s	Sail height
K_i	Ice plate stiffness
K_p	Passive earth pressure coefficient
k	Stiffness / safety factor
L	Distance between cylinders
l	Scour length
m	Mass
m_a	Added mass
m^*	Mass ratio
N	Normal force from seabed
P	Soil pressure
P_f	Frontal soil pressure
P_s	Side soil pressure
p	Pressure
Re	Reynolds number
St	Strouhal number
T	Period
T_b	Block size
t	Time
U_∞	Maximum velocity
U_c	Current velocity
U_i	Ice velocity
U_r	Reduced velocity
U_w	Wind velocity
U_*	Friction velocity
w_b	Width of the ice ridge at the bottom
w_t	Width of the ice ridge at the top
W	Weight of the ice ridge
W_c	Work of current drag force
W_{cx}	Work of horizontal passive friction force
W_{cy}	Work of vertical passive friction force
W_f	Work of driving force from surrounding floe
W_{fc}	Work of active friction force

W_w	Work of wind drag force
y	Vertical displacement

GREEK SYMBOLS

α_s	Sail angle
θ_k	Attack angle
β	Seabed slope
δ	Boundary layer thickness
μ	Dynamic viscosity / friction coefficient
ρ	Density
ρ_a	Air density
ρ_i	Ice density
ρ_{ia}	Ridge density in air
ρ_{iw}	Ridge density in water
ρ_s	Soil density
ρ_w	Water density
η	Sail porosity
ν	Kinematic viscosity / Poisson's ratio
τ	Non-dimensional time
φ	Internal friction angle
ϕ_w	Wall friction angle
γ	Submerged angle of response

1 INTRODUCTION

In recent years the Arctic zone, where significant resources of hydrocarbons have been discovered, is important for the oil and gas industry development. However, natural phenomena such as low temperatures, deep water and ice presence make the development of offshore fields much more challenging in the Arctic, particularly concerning the pipeline on-bottom protection.

The presence of the drifting ice often results in the formation of ice ridges. These ice ridges are able to make deep critical gouges on the seabed in shallow waters. The gouge depth may achieve 2-2.5 meters deep, depending on the strength of the soils. In this case all the subsea facilities have to be protected in order to prevent the interaction between ice ridges and equipment.

Another concern for pipeline integrity arises from pipeline vibrations: when a pipeline is submerged under water and has a free span, vortex-induced vibrations (VIV) appear and make the structure vibrate. Circular cylinders exposed to fluid flow perpendicular to their axis experience flow induced motions (FIM) excited by the alternating vortices shed in the cylinder wake that is forming the von Kármán vortex street. The cylinder would be excited to significant amplitudes when the vortex shedding frequency locks on to the vibration frequency (lock-in zone), thus synchronizing the natural frequency and the excitation frequency.

In this thesis the studying of the motions of cylindrical structures undergoing VIV is investigated by using numerical simulations. A numerical approach offers a few benefits. It allows performing parametric studies, where among a big number of influencing parameters one of them can be varied while the others are kept constant. This provides the ability to discern the functional dependencies governing the complex near-wall (near-bottom) VIV physics. Another benefit of numerical studies is the ability to go beyond the limitations of experimental facilities, which are often limited with respect to the maximum Reynolds number possible to achieve.

1.1 Frameworks and Scope of the Thesis

The thesis is focused on the pipeline that is laid from inshore to deep water at the Sakhalin region. The research includes the investigation of the ice ridge-seabed interaction in shallow waters and the investigation of the VIV phenomenon in deep waters. The pipeline protection by means of trenching and rock dumping is discussed as well.

The thesis has the following structure:

- Chapter 1: Introduction outlines the problem statement and the objectives of the thesis.

- Chapter 2: This chapter is dedicated to the Sakhalin region overview. It describes its features and gives the data concerning the temperatures, the current velocities and the water depth.

- Chapter 3: It describes the physics of the ice ridges, shows the ice scouring models and presents the load calculations.

- Chapter 4: The certain chapter is dedicated to CFD simulations of near-wall vortex-induced vibrations of pipelines at high Reynolds number.

- Chapter 5: It includes the methods of the pipeline on-bottom protection and the environmental assessment of protection methods.

- Chapter 6: Conclusions summarize the main aspects of the study and discuss the possible directions of a future investigation of the pipeline on-bottom protection, based on the current thesis.

- A comprehensive list of references is provided.

- Appendix A contains the detailed information about the calculation of ice scouring depth.

2 SAKHALIN REGION

Sakhalin Island is the largest island in Russian Federation, the total area is 76 600 km^2. Sakhalin is separated from the mainland by the Tatar Strait. The island stretches for 950 km from north to south. It is washed by two seas: the Sea of Okhotsk and the Sea of Japan. The island's water zone plays a significant role for Russia as it contains a big amount of undeveloped oil and gas deposits, and moreover, it is the major source of fishing.

2.1 Sakhalin Shelf Projects

Sakhalin island is an important administrative object as it has a variety of well-known mineral resources. The typical resources are energy-producing minerals such as oil, natural gas, coal. Sakhalin has a variety of both ferrous and non-ferrous metals, rare metals (mercury, tungsten, antimony) and rare-earth elements. The island's oil and gas industry is connected with a generalized name "Sakhalin shelf projects". Sakhalin shelf projects combine a group of projects for the development of hydrocarbon deposits on the continental shelf of the Sea of Okhotsk and the Sea of Japan and the Tatar Strait. In total, nine oil and gas fields (Figure 2.1) with total reserves of 1.2 trillion cubic meters of gas, 5 billion tons of oil were discovered on the Sakhalin shelf [13]. Table 2.1 shows the projects that are under development nowadays.
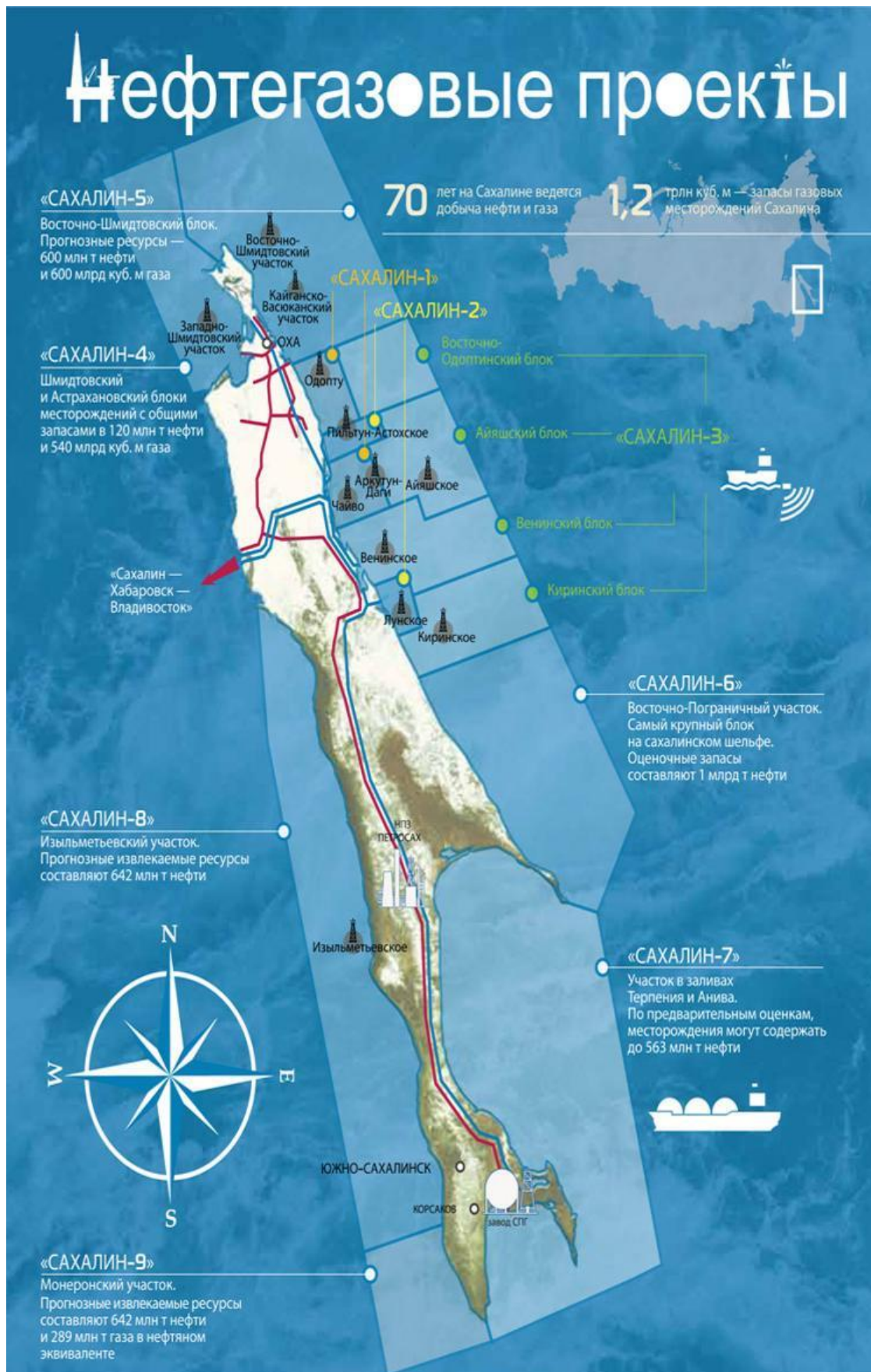
Figure 2.1 The overview of nine Sakhalin shelf projects [13]

Table 2.1 The active shelf oil and gas projects (Gudmestad et al., 1999)

Project	Operator	Oil and Gas filed	Water depth	Distance to shore	Main facilities
Sakhalin – 1	Exxon Neftegas Limited	Chayvo	20-25 m	10-13 km	Offshore Orlan platform Onshore Yastreb rig Chayvo onshore processing facility De-Kastri Terminal
		Odoptu	25-30 m	6-10 km	Onshore Yastreb rig Chayvo onshore processing facility
		Arkutun-Dagi	35-50 m	22-33 km	Berkut platform Chayvo onshore processing facility
Sakhalin – 2	Sakhalin Energy	Piltun-Astokhskoye	30 m	16 km	Piltun-Astokhskoye-A platform (Molikpaq) Piltun-Astokhskoye-B
		Lunskoye	50 m	13 km	Lunskaya-A platform
Sakhalin – 3	Gazprom	Kirinskoye	90 m	28 km	Subsea production facility Onshore processing facility

2.2 Ice Conditions at the Northeastern Shelf of Sakhalin Island

The ice conditions on the northeastern shelf of Sakhalin Island can be generally described as very harsh, it is the ice loads that are the most dangerous for the proposed facilities for the extraction and transportation of hydrocarbons.

During a winter, ice is observed in the waters of the northeastern Sakhalin shelf, which, by their characteristics, can be distinguished into a separate ice massif — the northeastern ice massif of Sakhalin Island. The Sea of Okhotsk is located in the monsoon climate zone of temperate latitudes, but for the northern part of the sea, which deeply extends into the Asian continent, some features of the climate of the Arctic seas are also typical. This also applies to the waters adjacent to the northern

part of Sakhalin Island. The monsoon climate is caused by a change in location and the nature of the interaction of large-scale pressure formations. An important role also plays the position of the island near the border of the Asian continent and the Pacific Ocean.

2.2.1 Duration of an Ice Season

Ice formation on the northeastern shelf of Sakhalin island begins in November, quickly spreading from north to south. In January, the first-year ice appears in the drift ice massif, shifting under the influence of currents and the prevailing winds of the northwestern rhumbs in the winter to the northeastern shelf from the northwestern part of the Sea of Okhotsk.

In March-April, the edge of the drifting ice reaches its maximum eastern position. From a middle of April, spring processes of breaking the ice cover begin to predominate, in May its intensive melting occurs and the processes of breaking up the ice fields continue. In June, young ice disappears, and only first-year ice is observed in the ice massif. By the end of June, there is a complete clearing of the water area of the northeastern shelf from ice (in the direction from south to north). According to Shevchenko et al. (2018), the duration of the ice period in the waters adjacent to the oil and gas fields of the Sakhalin-1 and Sakhalin-2 projects ranges from 160 to 210 days.

2.2.2 Formation of Heavy Ice on the Northeastern Shelf of Sakhalin Island

At the northeastern part of Sakhalin island at the beginning of winter ice processes are characterized by the intense ice formation due to the low air temperatures caused by the winds of the northern and northwestern temperatures characteristic of the winter season.

The ice that forms in the Sakhalin Bay is carried to the northeastern shelf of Sakhalin. This ice is rapidly moving along the coast to the south and it reaches the area of the location of the offshore ice-resistant platforms which are located at the Piltun-Astokhskoye field, the Chayvo and the Arkutun-Dagi fields and the Lunskoye

field (Figure 2.2). In the autumn, there is an increase in the longshore current to the south, caused by steady and fairly strong winds.

Figure 2.2 Lunskaya-A platform [14]

In the spring, ice has a considerable thickness and is in the stage of a destruction. During this period, offshore oil offloading operations and maintenance of drilling platforms are not conducted until ice concentration is predicted to be low for several days. Under the influence of the southeastern and southern winds of the established summer monsoon, the ice shifts towards the open sea and gradually melts there.

2.3 Meteorological Conditions

As Sakhalin region is considered to be sub-arctic zone, the climate is extremely severe. Strong winds are typical for this region which result to low temperatures and cause some difficulties for a field development. In summer air temperatures on the western coast of Sakhalin are higher than on the northeastern part of the island. The annual air temperatures at the Piltun-Astokhskoye field are shown in Table 2.2.

Table 2.2 Air temperature at Piltun-Astokhskoye field (Gudmestad et al., 1999)

Parameter	Air temperature at the Piltun-Astokhskoye field, °C											
	Jan	Feb	Mar	Apr	May	Jun	Jul	Aug	Sep	Oct	Nov	Dec
Average	-19.8	-17.8	-12.5	-4.2	0.6	4.9	9.6	13.1	10.3	4	-4	-15.4
Maximum	1	2	8	12	24	31	34	36	27	22	11	2
Minimum	-39	-38	-36	-30	11	-4	-1	3	-2	-15	-28	-35

Moreover, deep cyclones and typhoons at the northeastern coast of the island are considered to be typical. Calm weather is infrequent and doesn't exceed 20-30% and 50-60% in a winter period and a summer period, respectively. Wind velocities at the Piltun-Astokhskoye field are shown in Table 2.3.

Table 2.3 Wind velocity (m/s) appearing with n-year frequency (Gudmestad et al., 1999)

Average time	Frequency (years)				
	2	10	25	50	100
1 hour	25	32	34	28	41
1 minute	33	42	46	50	54
3 seconds	36	46	50	55	59

2.4 Hydrological Conditions

The general scheme of the circulation of the waters of the Sea of Okhotsk combines different types of water, which leads to uneven distribution of the flow velocities throughout the basin. According to statistics [11], the average value of the velocity of the currents on the northeastern shelf is 50-90 cm/s, and the maximum value is 360 cm/s.

3 ICE RIDGES

This chapter is dedicated to ice ridges at Sakhalin region. It includes the nature of an ice ridge formation, theoretical approaches of ice scouring calculation, initial parameters for ice scouring calculations. Further results and main conclusions are given.

3.1 Morphology of Ice Ridges

Generally, a sea ice on average consists of 10-40% ridges by volume. Floating ice due to winds and currents is more dynamic and is subjected to drift. Drifting ice may break resulting in ice deformation by two common mechanism: ridging and rafting. Ridging presents the interaction of two floes or sheets at their edges and rafting is related to the submersion of one ice floe or sheet beneath another. The present study investigates only first-year ridged.

Ice ridges generally consist of three main parts (Figure 3.1):

- The sail that is above the water surface.
- The consolidated layer that is below the water line and presents the blocks that are fully frozen to each other.
- The rubble that is located under the consolidated layer and consists of blocks partially frozen together.

The consolidated layer and the rubble create together the keel.
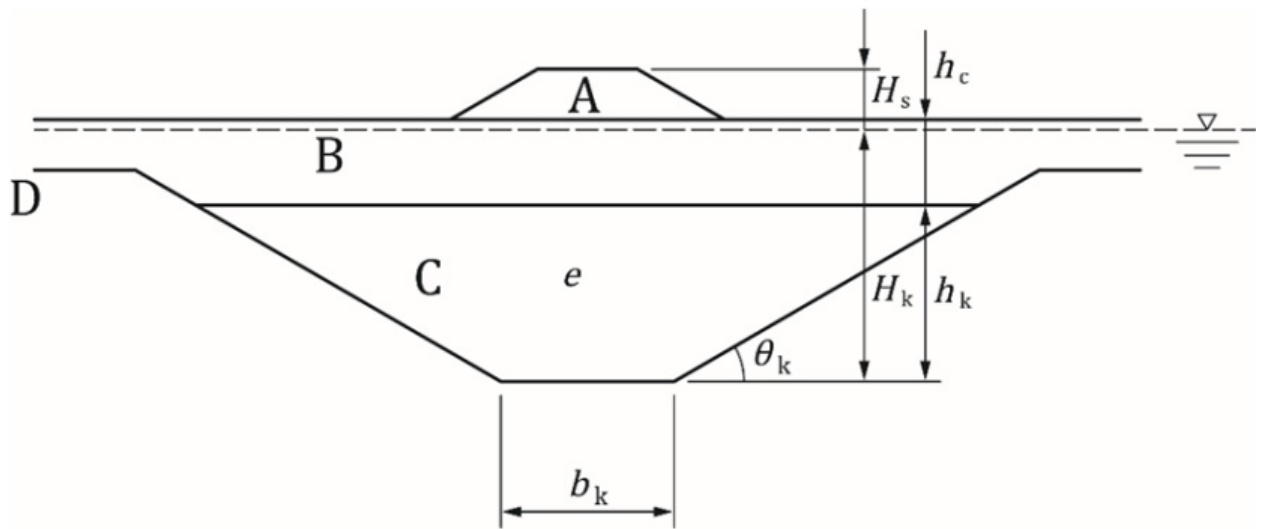
Figure 3.1 Model of a first-year ice ridge. A – sail; B – consolidated layer; C – rubble; D – level ice. (ISO 19906, 2019)

Ice ridges can be divided into pressure ridges and shear ridges. Pressure ridges are formed by one ice floe or sheet moving into another and they are able to exist as single features. The form of keel and sail is often triangular or trapezoidal. Shear ridges are caused by one ice floe or sheet sliding along another's edge.

First-year ice ridges have porous space that consists of ice air, water, snow and ice. The sail is filled with air and snow, while the keel consists of water and air in some cases.

A triangular keel is formed when ice sheets interact to each other directly resulting in formation of rubbles on top and below the sheets (Figure 3.2). The feature of this type of a ridge keel is the fact that the consolidated layer may be a solid ice sheet. It happens when the main ice sheet forms the beginning of the consolidated layer that differs from a rubble field formation where the consolidated layer has a porous media. According to Obert et al. (2011) the triangular shape is characterized by a large w_t/w_b ratio that is 6.5 in average. A typical triangular keel is shown in Figure 3.3.
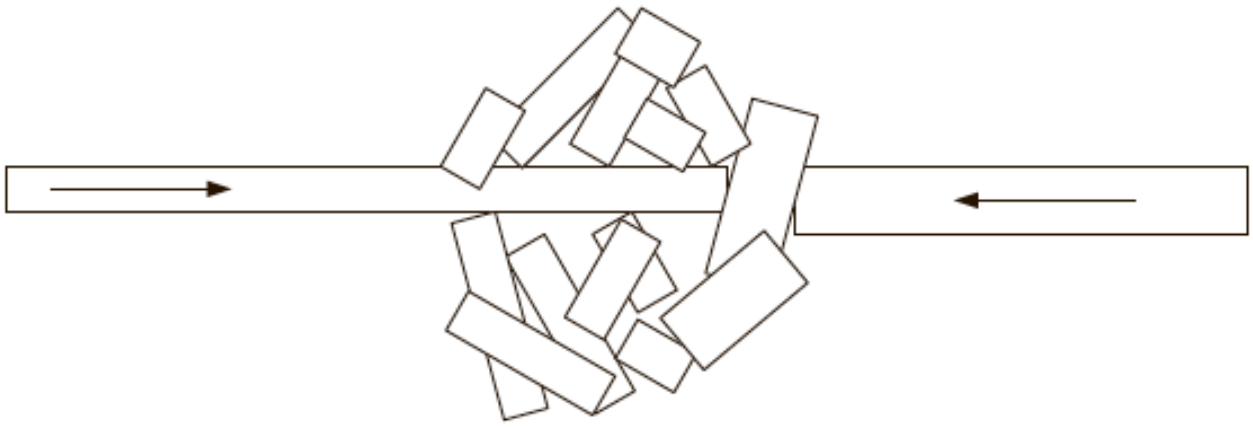
Figure 3.2 Diagram of a single keel formation (Obert and Brown, 2011)
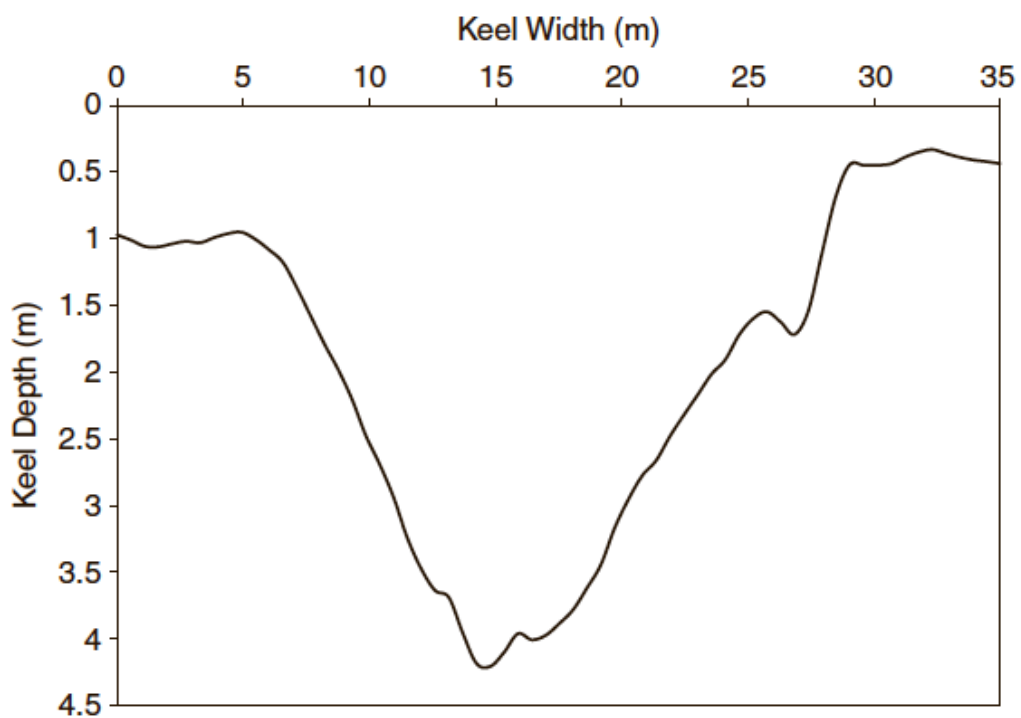
Figure 3.3 Typical triangular keel (Obert and Brown, 2011)

Trapezoidal keels (Figure 3.4) have steep keel angles, as their bottom are almost flat and wide. Generally, trapezoidal keels are formed due to a triangular keel becomes to grow laterally resulting in a wide and shallow keel.

11
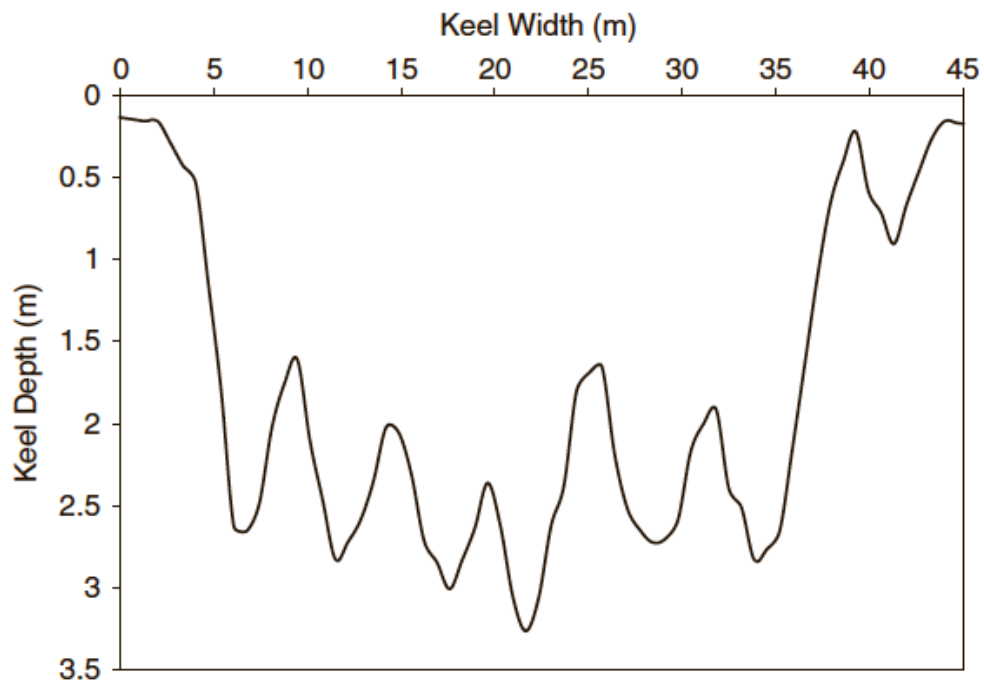
Figure 3.4 Typical trapezoidal keel (Obert and Brown, 2011)

Multiple peak keels can be defined as a keel with a several peaks each of which has approximately the same depth (Figure 3.5). Multiple peak keels are created from a rubble field and can be formed in two different ways:

1. Two ice sheets with different thickness collapse and create random rubbles, which in their turn form more random peaks (Figure 3.6).
2. A few triangular keels are combined together forming a new overlapping keel.
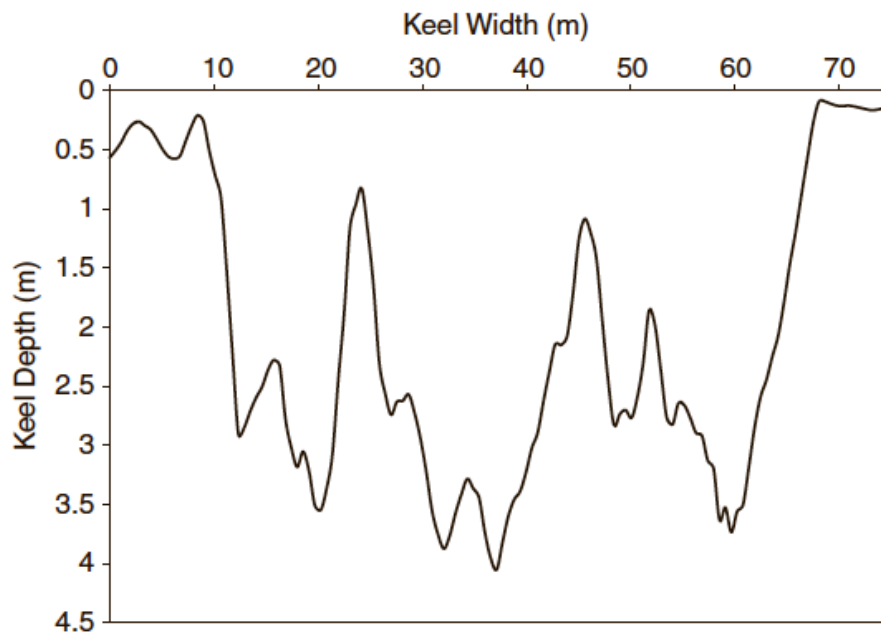
Figure 3.5 Typical multiple peak keel (Obert and Brown, 2011)
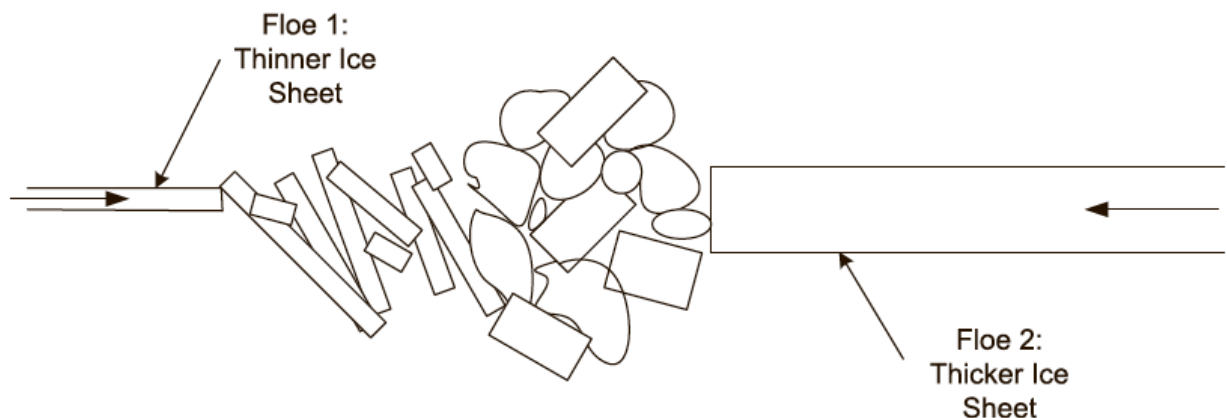
Figure 3.6 Formation of a multiple peak keel (Obert and Brown, 2011)

3.2 Ice Scouring

Various drifting ice formations may cause different damages on submerged structures depending on the water depth and the keel draft. The following damage types are the most common for subsea structures:

- Damage of the subsea completion system;
- Subsea pipelines ruptures and damage;
- Disruption of the cable communication system;
- Damage of the stationary ice resisting equipment.

13

According to Vershinin et al. (2008), there are four possible schemes of the ice ridge interaction with the soil.

Scheme 1 (Figure 3.7 (a)) describes the situation when the rotation of the moving floe is eliminated that is the system has only one degree of freedom. Due to additional restrictions on rotation, the present scheme assumes the significant increase of the load on seabed and refers to the maximum gouge depth.

Scheme 2 (Figure 3.7 (b)) considers the possible ridge upward movements due to the flexural strength of the ice sheet. The current scheme suits for situations when the ice cover has a significant rigidity and thickness.

Scheme 3 (Figure 3.8) considers the rotation of the ice formation making it more realistic.

Scheme 4 corresponds to an ice formation model where an ice cover has a small bending capacity and, moreover, there are crevices around the level ice field (Figure 3.9 (a)). Due to the bending moment caused by the ridge vertical movement and rotation the contact sections may be destroyed and the model of an ice ridge calculation will be totally changed (Figure 3.9 (b)).
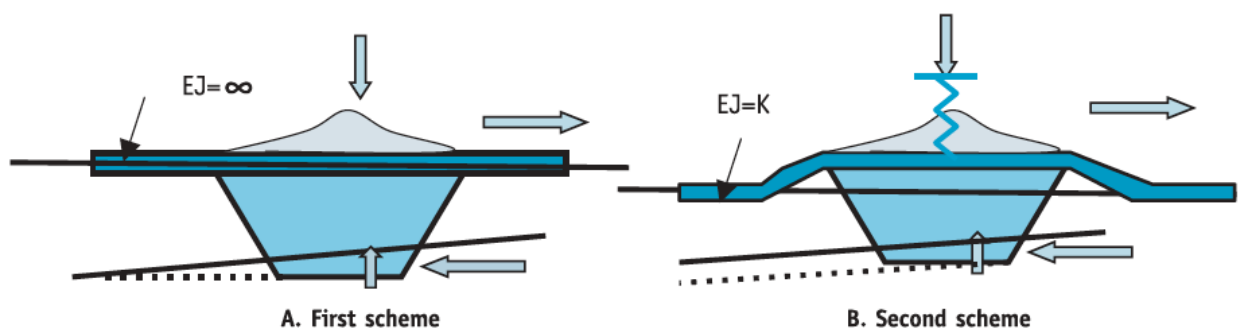
Figure 3.7 Schemes of an ice ridge interaction (Vershinin et al., 2008)
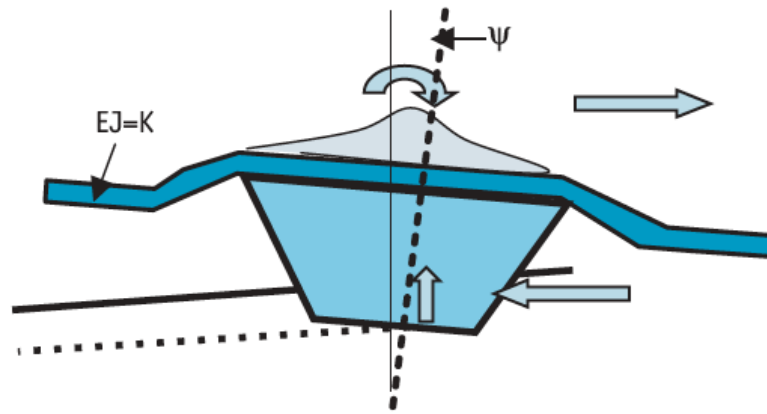
Figure 3.8 The movement scheme of a jammed ridge (Vershinin et al., 2008)
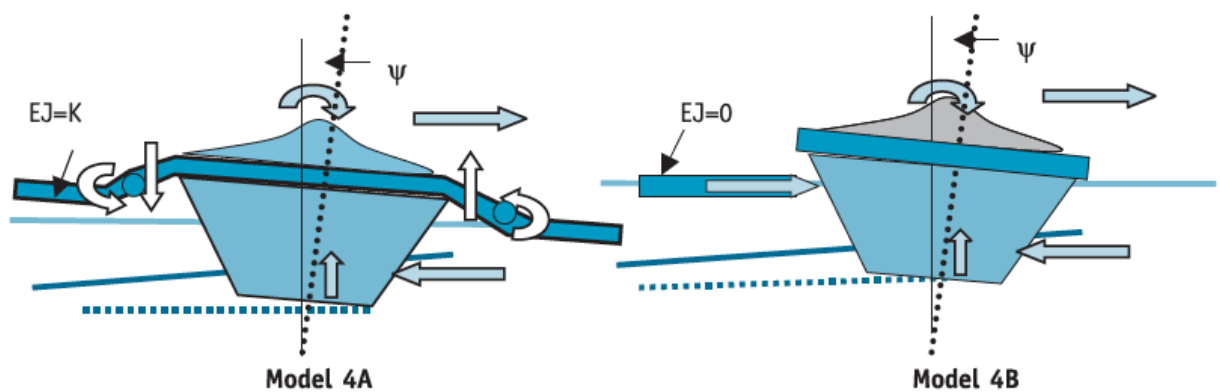
*Figure 3.9 Ice field destruction scheme at appearance of a rotational torque and a vertical displacement
(Vershinin et al., 2008)*

3.3 Initial Parameters

The certain thesis uses two different approaches for the scour depth calculations: force model and energy model. In order to present the critical scour depth in Sakhalin region, the following initial parameters are used. Presented initial parameters are critical for the northeastern shelf of Sakhalin island and are taken from published statistic data [30, 11].

Table 3.1 Initial parameters for ice scouring calculations

Property	Parameter	Symbol	Value	Unit
Ice	Sail height	h_s	1.6	m
	Level ice thickness	h	4	m
	Consolidated layer thickness	h_c	6	m
	Ridge breadth	B	20	m
	Attack angle	θ_k	30	°
	Sail angle	α_s	20	°
	Block size	T_b	0.4	m
	Ice density	ρ_i	910	kg/m^3
	Ice velocity	U_i	1.1	m/s
	Sail porosity	η	0.07	—
	Elasticity modulus	E	8	GPa
	Poisson's ratio	ν	0.34	—
Soil	Internal friction angle	φ	30	°
	Wall friction angle	ϕ_w	25	°
	Friction between ice and soil	μ	0.5	—
	Soil density	ρ_s	1500	kg/m^3
	Seabed slope	β	1	°
Environments	Water density	ρ_w	1030	kg/m^3
	Air density	ρ_a	1.3	kg/m^3
	Current velocity	U_c	3.6	m/s
	Wind velocity	U_w	30	m/s
	Current drag coefficient	C_{dc}	0.9	—
	Wind drag coefficient	C_{dw}	0.9	—
	Wind skin coefficient	C_{sw}	0.001	—

3.4 Force Scouring Model

The certain scheme of scouring calculation is based on the equilibrium of forces when the ice ridge is in direct contact with the seabed. The scheme of force application is shown in Figure 3.10.

In order to investigate the certain scheme for ice scouring depth, the following assumptions should be applied:

- The force model corresponds to scheme 1 (Figure 3.7 (a));
- Vertical displacement of an ice ridge is excluded;
- Angle between an ice ridge and the seabed corresponds to the attack angle.
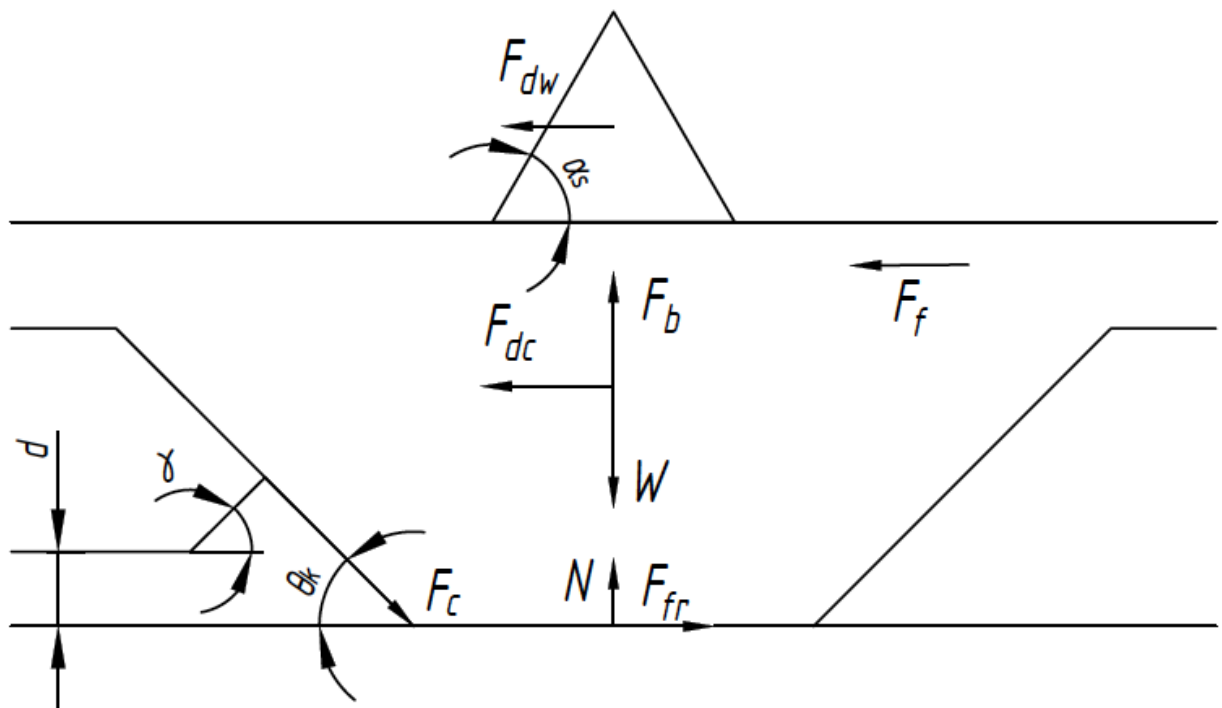
Figure 3.10 Scheme of acting forces

In Figure 3.10 F_b – buoyancy force; W – weight of the ice ridge; F_{dc} and F_{dw} are drag force from current and wind, respectively; F_{fr} – friction force of the ice ridge; N – normal force from seabed; F_f – force from surrounding floe; F_c –

Coulomb's friction force; θ_k – attack angle; α_s – sail angle; γ – submerged angle of response; d – gouge depth.

The equilibrium equations in both directions are obtained as:

$$F_{dc} + F_{dw} + F_f - F_{fr} - F_c \cdot \cos\theta = 0 \tag{3.1}$$

$$F_b - W + N - F_c \cdot \sin\theta = 0 \tag{3.2}$$

Drag force from wind F_{dw} consists of two components: frontal and top (skin effect), and is defined as:

$$F_{dw} = 0.5 \, C_{dw}\rho_a A_{w1} U_w^2 + 0.5 \, C_{sw}\rho_a A_{w2} U_w^2 \tag{3.3}$$

where C_{dw} – drag coefficient from wind, ρ_a – air density, U_w – wind velocity, C_{sw} – wind skin coefficient.

The projected areas A_{w1} and A_{w2} are given as:

$$A_{w1} = \left(h_s - \frac{\rho_w - \rho_i}{\rho_w} h \right) \cdot B \tag{3.4}$$

$$A_{w2} = b_w B \tag{3.5}$$

Drag force from current F_{dc} is defines as:

$$F_{dc} = 0.5 \, C_{dc}\rho_w A_c U_c^2 \tag{3.6}$$

where C_{dc} – drag coefficient from current, ρ_w – water density, U_c – current velocity.

The projected area A_c is given as:

$$A_c = \left(h_k - \frac{\rho_i}{\rho_w} h \right) \cdot B \tag{3.7}$$

In order to calculate the weight of the ice ridge it is necessary to consider the density dissimilarity and shape difference. In this case the ice ridge weight consists of three parts: weight of the sail, weight of the rectangular consolidated layer and weight of the lower trapezoidal part. Thus, weight of the ice ridge is calculated as:

$$
\begin{aligned}
W = \rho_{iw} B g \cdot \Bigg[&\frac{\rho_{ia}}{\rho_{iw}} \left(h_s - \frac{\rho_w - \rho_i}{\rho_w} h_c \right)^2 \cot\alpha_s + \frac{\rho_i}{\rho_{iw}} h_c b_w \\
&+ 0.5 \, (b_w + b_k) \left(h_k - \frac{\rho_i}{\rho_w} h_c \right) \Bigg]
\end{aligned}
\tag{3.8}
$$

Buoyancy force F_b influence only submerged parts of the ice ridge, so it is expressed as:

$$F_b = \rho_w B g \cdot \left[0.5\,(b_w + b_k)\left(h_k - \frac{\rho_i}{\rho_w}h_c\right) + \frac{\rho_i}{\rho_w}h_c b_w\right] \qquad (3.9)$$

According to Vershinin et al. (2008), the maximum driving force from surrounding floe F_f (MN) can be calculated as:

$$F_f = 0.43 \cdot 4.059 \cdot \left(\frac{B}{h}\right)^{-0.378} \cdot h^{-0.75} \cdot B \cdot h \qquad (3.10)$$

Passive friction force according to soil mechanics theory is defined as:

$$F_c = \mu P cos\phi_w \qquad (3.11)$$

where μ – friction coefficient between ice ridge and soil, P – soil pressure, ϕ_w – wall friction angle.

Soil pressure P_f acting in front of the ridge is defined as:

$$P_f = 0.5\,K_p \rho_s g (h_1 + d)^2 B \qquad (3.12)$$

where K_p – passive earth pressure coefficient, ρ_s – soil density, h_1 – frontal mound height, d – gouge depth, B – ridge breadth.

$$K_p = \frac{\cos^2 \varphi}{\cos \phi_w \left[1 - \sqrt{\dfrac{\sin(\varphi + \phi_w) \cdot \sin(\varphi)}{\cos \phi_w}}\right]^2} \qquad (3.13)$$

Soil pressure P_s for side resistance is defined as:

$$P_s = \frac{1}{6}K_p \cdot \rho_s \cdot g \cdot d^2 \cdot b_k (b_k + d \cdot \cot \theta_k) \qquad (3.14)$$

Thus, Coulomb's friction force for each direction is calculated as:

$$F_{cx} = F_c \cdot \cos \theta_k = \mu P_f \cos \phi_w \cos \theta_k + \mu P_s \cos \phi_w \qquad (3.15)$$

$$F_{cy} = F_c \cdot \sin \theta_k = \mu P_f \cos \phi_w \sin \theta_k \qquad (3.16)$$

The calculations are presented in Appendix A.

3.5 Energy Scouring Model

The energy approach is based on the kinetic energy transfer from the ice ridge to soil from the point of their direct contact. Acting forces change consequently since the initial ice ridge velocity drops until the complete stop.

For energy model calculation the following assumptions are applied:

- Energy scouring model corresponds to scheme 2 (Figure 3.7 (b));
- The level ice is rigid enough that allows the ice ridge to make vertical displacement without destroying the ice field;
- Initially the ice ridge moves with velocity U_i, that is decreasing during ice scouring;
- Vertical displacement of the ice ridge is the linear function of the ice scouring length;
- Projected areas of drag forces remain constant despite the vertical displacement.

The energy balance equation is defined as:

$$E_k + W_w + W_c + W_f = W_{fr} + W_{cx} + W_{cy} + E_p + E_i \qquad (3.17)$$

where E_k – ridge kinetic energy, W_w – work of wind drag force, W_c – work of current drag force, W_f – work of driving force from surrounding floe, W_{fr} – work of active friction force, W_{cx} – work of horizontal passive friction force, W_{cy} – work of vertical passive friction force, E_p – ridge potential energy, E_i – ice field potential energy.

Ridge kinetic energy is known as:

$$E_k = \frac{W U_i^2}{2g} \qquad (3.18)$$

Wind and current drag forces depend on the scour length l: at the beginning they have minimum value, further the forces increase monotonously until the ridge stops. In this case wind and current drag forces are defined as:

$$F_{dw} = 0.5\, C_{dw}\rho_a A_{w1}\left(U_w - \frac{l-x}{l}U_i\right)^2$$

$$+\, C_{sw}\rho_a A_{w2}\left(U_w - \frac{l-x}{l}U_i\right)^2 \tag{3.19}$$

$$F_{dc} = 0.5\, C_{dc}\rho_w A_c\left(U_c - \frac{l-x}{l}U_i\right)^2 \tag{3.20}$$

As the submerged volume decreases, the buoyancy force changes continuously as well and is approximated according to Duplenskiy (2012) as:

$$F_b = \rho_w g B\left[(15.44 h_s - 3.95 h_s \tan\theta_k)\left(3.95 h_s - \frac{\rho_i}{\rho_w}h_c\right)\right.$$

$$\left. +\, 15.44\frac{\rho_i}{\rho_w}h_c h_s - b_w y\right] \tag{3.21}$$

Ice driving force from surrounding floe is given as:

$$F_f = \frac{x}{l}\,0.43 \cdot 4.059 \cdot B^{0.622} \cdot h^{0.628} \tag{3.22}$$

Passive earth pressure acting both on the front face and side face for the energy approach is outlined by Choi el al. (2002) as:

$$P_f = 0.5\, K_p \rho_s g B[(1 + C_1 \tan\beta)(h_1 + x\tan\beta - y)]^2 \tag{3.23}$$

$$P_s = \frac{1}{6}K_p \rho_s g \cot\beta\,(x\tan\beta - y)^3 \tag{3.24}$$

$$C_1 = \frac{\cot\theta_k}{1 - \cot\theta_k \tan\beta} \tag{3.25}$$

$$d = x\tan\beta - y \tag{3.26}$$

Due to equations above, passive friction force is calculated as:

$$F_c = \mu P \cos\phi_w \tag{3.27}$$

$$F_{cx} = \mu P_f \cos\phi_w \cos\theta_k + \mu P_s \cos\phi_w \tag{3.28}$$

$$F_{cy} = \mu P_f \cos\phi_w \sin\theta_k \tag{3.29}$$

As the ice ridge elevates, it causes bending of the level ice. In order to calculate the tension force, an elasticity theory is applied.

$$F_t = k_i \cdot y \tag{3.30}$$

$$k_i = \left[\frac{Eh^3\rho_w g}{24(1-v^2)}\right]^{0.5} \tag{3.31}$$

where F_t – tension force of ice field, k_i – ice plate stiffness, y – vertical displacement, E – ice elasticity modulus, v – Poisson's ratio.

Considering changes in buoyancy force F_b and tension force F_t, active friction force is adopted as:

$$F_{fr} = \mu N(y) = \mu\left[W - F_b(y) + F_t(y) + F_{cy}(y)\right] \tag{3.32}$$

$$F_{fr} = \mu\left[\rho_w g B b_w y + F_t(y) + F_{cy}(y)\right] \tag{3.33}$$

Ice ridge potential energy is expressed as:

$$E_p = \int_0^{\delta(l)} (W - F_b)dy = \int_0^{\delta(l)} \rho_w g B b_w y \, dy = \frac{\rho_w g B b_w \delta(l)^2}{2} \tag{3.34}$$

Ice field potential energy is a function of the ice ridge vertical displacement $\delta(l)$, as the ridge elevates, it causes stresses due to surrounding floe bending.

$$E_i = \int_0^{\delta(l)} k_i y \, dy = \frac{k_i \delta(l)^2}{2} \tag{3.35}$$

The calculations are made using Matlab program and are presented in Appendix A.

3.6 Model Validation

Within the framework of this thesis, the ice scouring calculations are conducted using two different methods: force and energy methods. The obtained results are compared with similar experiments and shown in Table 3.2.

Table 3.2 Comparison of study results with other experiments

Experiment	Description	Scour depth, m	Scour length, m
Present study	Force model	2.58	-
	Energy model	1.96	170.9
Duplenskiy (2012)	Force model	2.26	
	Energy model	1.78	
Choi et al. (2002)	Free floating ridge	0.78	
Vershinin et al. (2008)	Ice confined ridge	1.84	

Bases on obtained results, the energy model approach is more reliable and accurate. The scour depth calculated for Sakhalin region fits the results gained by Vershinin et al. (2008) and Duplenkiy (2012). It means that the model is validated and the results are considered to be realistic.

3.7 Summary

Based on conducted research, the following conclusions can be formed:

- Generally, forms of ice ridges are divided into three main groups: triangular, trapezoidal and multipeak ridges. Moreover, there are four possible schemes of the ice ridge interaction with soil. All the possible scenarios have to be calculated in order to predict the scour depth and protect pipelines and subsea equipment against possible damage;

- Compared to earlier conducted experiments, the energy model of ice gouging provides more accurate results than the force model;

- Based on the experimental data, given in Table 3.2, the possible scour depth is 1.96m, which means that the pipeline protection by means of trenching should be implemented.

4 CFD SIMULATIONS OF NEAR-WALL VORTEX-INDUCED VIBRATIONS OF PIPELINES AT HIGH REYNOLD NUMBER

The certain chapter is dedicated to vortex-induced vibrations. It contains the theory about the formation of vortex-induced vibrations, the description of CFD simulation setup, the model of VIV investigation, and finally, the results and discussions are given.

4.1 Theory

4.1.1 Flow Regime

The Reynolds number is a dimensionless parameter that describes the flow pattern and is governed as:

$$Re = \frac{DU}{\nu} \qquad (4.1)$$

where D is the diameter, ν is the kinematic viscosity and U is the flow velocity. The flow changes considerably as the Reynolds number increases from zero. Figure 4.1 describes how the flow changes in dependence to the Reynolds number (Sumer and Fredsøe, 2006).
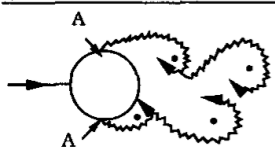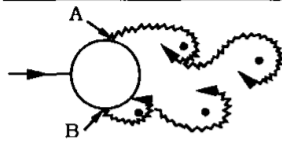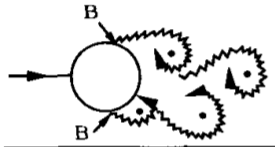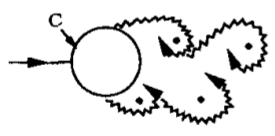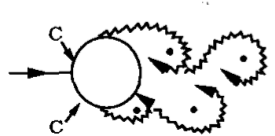
	Description	Reynolds number
a)	No separation. Creeping flow	$Re < 5$
b)	A fixed pair of symmetric vortices	$5 < Re < 40$
c)	Laminar vortex street	$40 < Re < 200$
d)	Transition to turbulence in the wake	$200 < Re < 300$
e)	Wake completely turbulent. A: Laminar boundary layer separation	$300 < Re < 3 \times 10^5$ Subcritical
f)	A: Laminar boundary layer separation B: Turbulent boundary layer separation; but boundary layer laminar	$3 \times 10^5 < Re < 3.5 \times 10^5$ Critical (Lower transition)
g)	B: Turbulent boundary layer separation; the boundary layer partly laminar partly turbulent	$3.5 \times 10^5 < Re < 1.5 \times 10^6$ Supercritical
h)	C: Boundary layer completely turbulent at one side	$1.5 \times 10^6 < Re < 4 \times 10^6$ Upper transition
i)	C: Boundary layer completely turbulent at two sides	$4 \times 10^6 < Re$ Transcritical

Figure 4.1 Flow regimes around a circular cylinder in steady current (Sumer and Fredsøe, 2006)

When the Reynolds number is very small ($Re < 5$), there is no separation. In the range $5 < Re < 40$ separations appear in the shape of a fixed pair of vortices in the trace of a cylinder. At $Re = 40$ the phenomenon of vortex shedding, when the wake becomes unstable, occurs. Vortices are shed one by one from each cylinder side at a certain frequency and a vortex street appears in the cylinder wake.

When the Reynolds number varies in the range $40 < Re < 200$, the vortex street is considered to be laminar. In this case the shedding is two-dimensional as there are no variations in the spanwise direction. (Sumer and Fredsøe, 2006).

With the further increase of the Reynolds number three-dimensional effects are significant due to transition to turbulence forms in the wake $(200 < Re < 300)$ and moves toward the cylinder. At $Re > 300$ regime the wake is characterized as completely turbulent. For $300 < Re < 3 \times 10^5$ this regime is denoted as the subcritical flow regime, because the boundary layer remains laminar over the cylindrical surface. As the Reynolds number continues increasing, the transition to turbulence takes place in the area of the boundary layer. At the separation point the layer becomes turbulent, but only at one side of the cylinder causing an asymmetric mean lift. This flow regime is known as the lower transition regime or the critical flow regime $(3 \times 10^5 < Re < 3.5 \times 10^5)$.

At the range $3.5 \times 10^5 < Re < 1.5 \times 10^6$ the boundary layer is turbulent at both sides of the cylinder, however, the transition process has not been finished yet as the transition occurs between the stagnation and separation points. This type of regime is called supercritical flow regime.

The next stage is known as the upper-transition regime that is created at the range $1.5 \times 10^6 < Re < 4.5 \times 10^6$. In this case when the Reynolds number reaches the value of 1.5×10^6, the boundary layer is considered to be fully turbulent at one side and partly turbulent and partly laminar at the other side.

When the Reynolds number exceeds the value of 4.5×10^6 the boundary layer around the cylinder is completely turbulent everywhere and this regime is called the transcritical regime.

4.1.2 Mechanism of Vortex Shedding

Vortex shedding is a feature that is present in all flow regimes for $Re > 40$. This phenomenon is a result of the instability existing between two free shear layers formed from the separation point into downstream flow.

As mentioned above the pair formed by two vortices is unstable, therefore, one vortex will be larger than the other one. The larger vortex draws the opposite one across the wake. The direction of the lager vortex is clockwise while the direction of the other vortex is anti-clockwise. When the smaller vortex approaches the opposite site, it will cut off the dominating vortex from its boundary layer (Figure 4.2 (a)). After the vortex is shed and free it is convected downstream in the wake. Then a new vortex will be created and the drawn vortex being the dominant one will become larger so that it will draw newly formed vortex on the opposite side (Figure 4.2 (b)). The whole cycle continues on the opposite side of the cylinder and leads to the repeated shedding of the vortices in the wake.
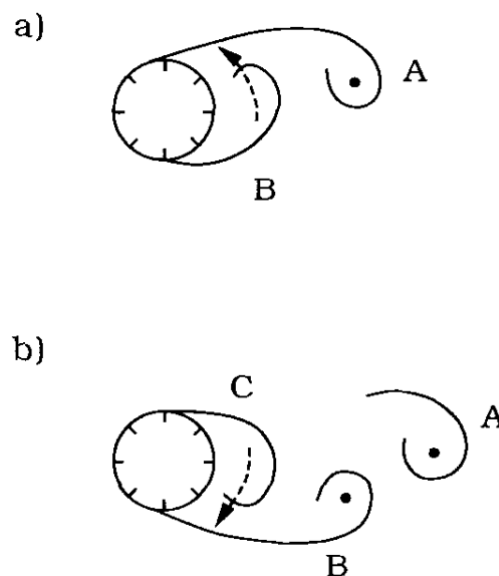
Figure 4.2 Vortex shedding mechanism (Sumer and Fredsøe, 2006)

4.1.3 Hydrodynamic Forces

The resultant force that acts on the cylinder can be divided into two contributions, one from the friction and the other from the pressure. The mean value of pressure and friction forces in each direction (in-line and cross-flow) can be calculated by integrating the pressure $\overline{p}$ and the wall shear stress $\overline{\tau}$ on the surface of the cylinder:

$$\overline{F_p} = \int_0^{2\pi} \overline{p} \cos(\phi) \, r_0 d\phi \qquad (4.2)$$

$$\overline{F_f} = \int_{0}^{2\pi} \overline{\tau} \cos(\phi) \, r_0 d\phi \qquad (4.3)$$

The total in-line force is called mean drag $\overline{F_D}$ and is obtained as the sum of the form drag $\overline{F_p}$ and the friction drag $\overline{F_f}$:

$$\overline{F_D} = \overline{F_p} + \overline{F_f} \qquad (4.4)$$

The total cross-flow force is called mean lift $\overline{F_L}$ and is defined in a similar way. Due to the symmetry in the flow the $\overline{F_L}$ will be zero, but when vortex shedding occurs, the mean lift force is non-zero.

As the vortex shedding phenomenon starts developing, the pressure distribution around the cylinder changes periodically and it results in a periodic variation of forces. In Figure 4.3 it is shown how forces change throughout a time-series. The drag force acting in the in-line direction oscillates around the mean drag, while in the cross-flow lift force is non-zero though the flow is symmetric.
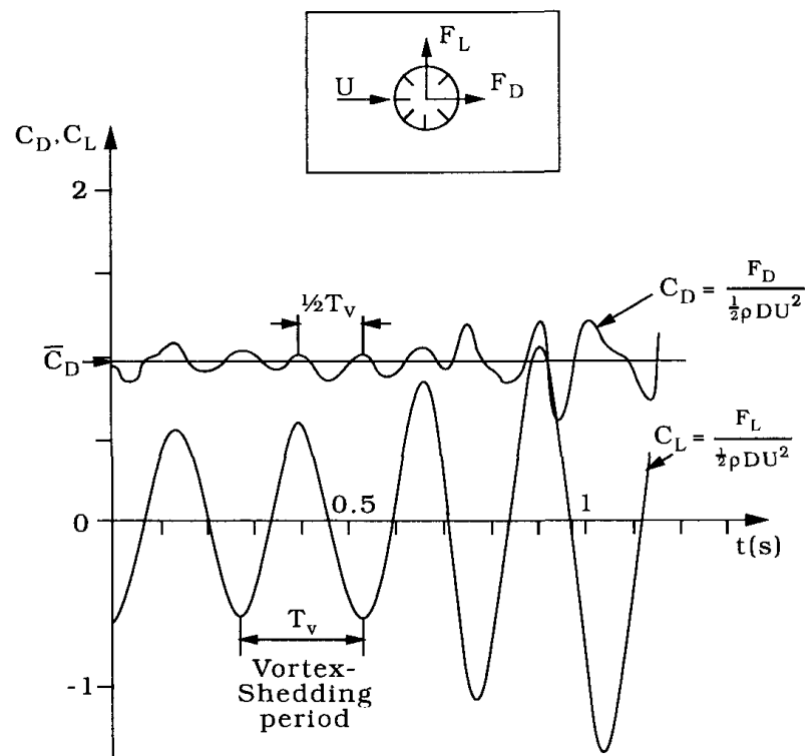
Figure 4.3 Drag and lift forces (Sumer and Fredsøe, 2006)

4.1.4 Drag and Lift Coefficients

The general equation for the drag force can be expressed as:

$$\frac{\overline{F_D}}{0.5\ \rho D U^2} = \int_0^{2\pi} \left[\left(\frac{\overline{p}-p_0}{\rho U^2}\right)\cos(\phi) + \left(\frac{\overline{\tau_0}}{\rho U^2}\right)\sin(\phi) \right] d\phi \qquad (4.5)$$

The right-hand side is known as the drag coefficient $\overline{C_D}$ and is the function of the Reynold number (Figure 4.4).

Thus, the drag and lift coefficients are denoted as:

$$\frac{\overline{F_D}}{0.5\ \rho D U^2} = \overline{C_D} \qquad (4.6)$$

$$\frac{\overline{F_L}}{0.5\ \rho D U^2} = \overline{C_L} \qquad (4.7)$$

where $\overline{F_D}$ is the mean drag force, $\overline{F_L}$ is the mean lift force, ρ is the fluid density, D is the projected area orthogonal to the flow (in the case of a pipe it is the diameter of the pipe), U is the velocity of the flow.
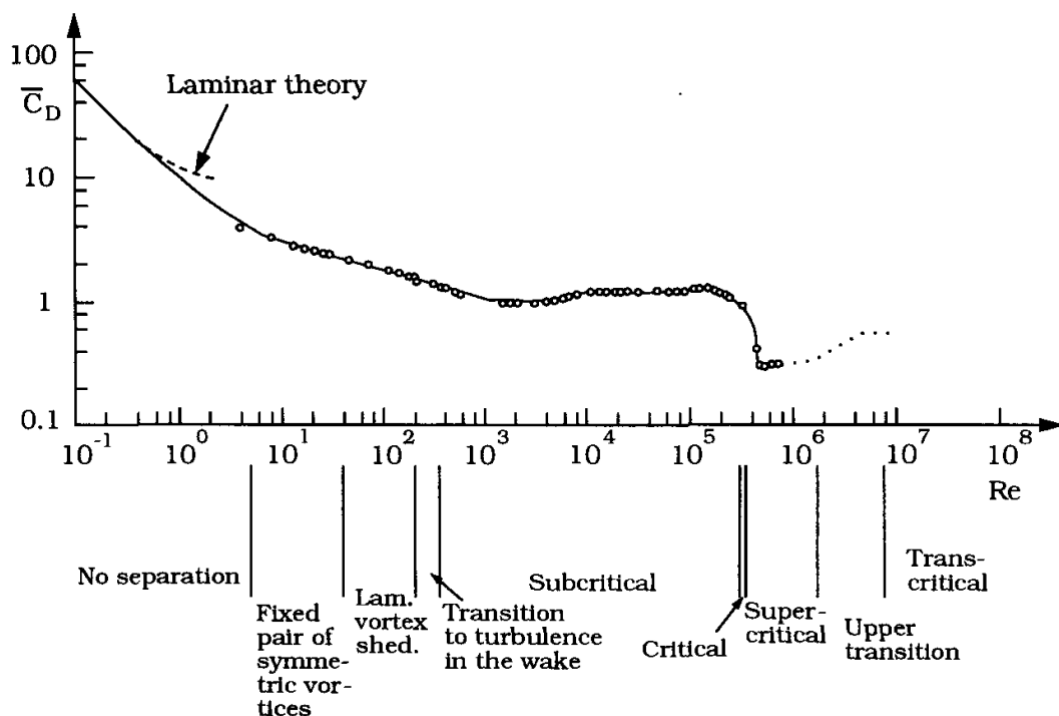
Figure 4.4 The dependency of the drag coefficient and the Reynold number for a smooth cylinder (Sumer and Fredsøe, 2006)

29

In Figure 4.4 $\overline{C_D}$ decreases monotonously until it reaches the Re value of about 300. For the range $300 < Re < 3 \times 10^5$ the drag coefficient has nearly constant value, but further it has a dramatic drop. This fall in $\overline{C_D}$ is named as the drag crisis.

4.1.5 Interaction Parameters

The certain group of dimensionless parameters are related to the interaction between the structure and the fluid around it.

The response of the cross-flow vibrations is expressed as non-dimensional amplitude (for in-line direction this parameter is defined in the similar way):

$$\frac{A}{D} \tag{4.8}$$

The path length of a vibrating body can be denoted as a ratio between the distance of the flow per one cycle U/f. In order to normalize it should be divided by the characteristic dimension (in the case of a cylinder it is D). This ratio is called the reduced velocity and is given:

$$U_r = \frac{U}{f_n D} \tag{4.9}$$

where f_n is the natural frequency of the system in still water.

Another important parameter is the Strouhal number St. It is a dimensionless parameter that is defined as the ratio between the vortex shedding frequency and the flow velocity divided by the characteristic dimension U/D:

$$St = \frac{f_{st} D}{U} \tag{4.10}$$

The Strouhal number is the function of the Reynolds number (Figure 4.5). In the range $40 < Re < 300$ the Strouhal number increases from 0.1 to 0.2 and further remains practically constant until reaches the critical regime. The dramatic increase of the Strouhal number is connected with changes of the boundary-layer characteristics and relocation of the separation points.
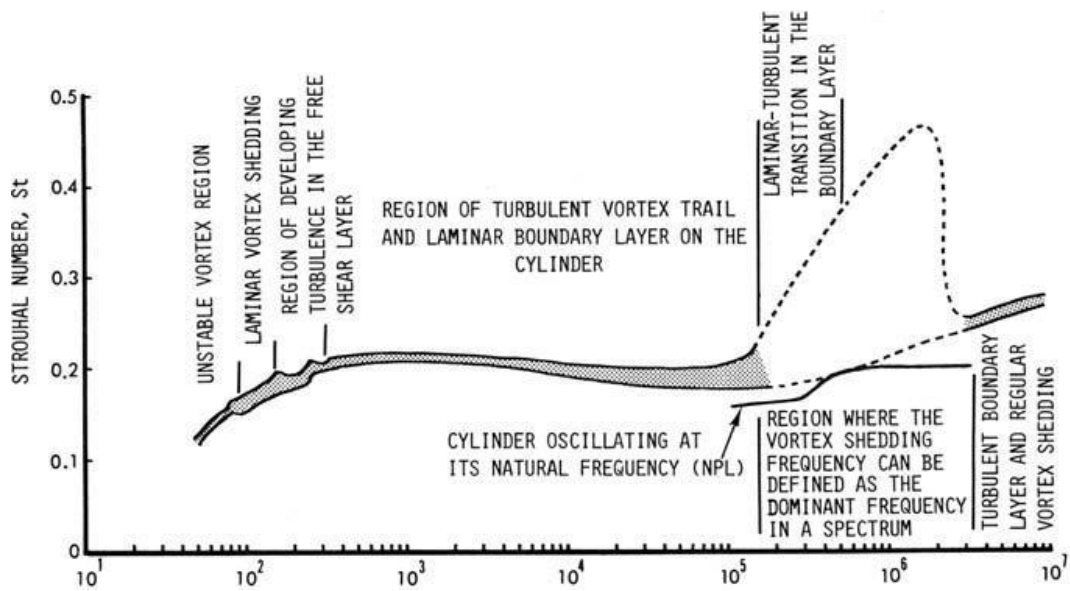
Figure 4.5 The relationship between the Strouhal number and the Reynolds number (Sarpkaya, 2010)

4.1.6 Lock-in

A series of experiments concerning the cross-flow vibrations of a circular cylinder shows that while the velocity of the flow increases from zero, there is no vibrations until the reduced velocity reaches the approximate value of $U_r = 4$. Further the vibrations occur and follow the Strouhal law (Figure 4.6). As $U_r = 5$ the oscillation frequency f_{osc} departs from the Strouhal frequency f_{st} and remains to be equal the natural frequency of the system $\frac{f}{f_n} \approx 1$. This phenomenon is known as the lock-in phenomenon. In the lock-in range the oscillation frequency increases monotonously as the natural frequency of the system depends on the added mass

$$f_n = \frac{1}{2\pi} \sqrt{\frac{k}{m+m_a}} \,.$$
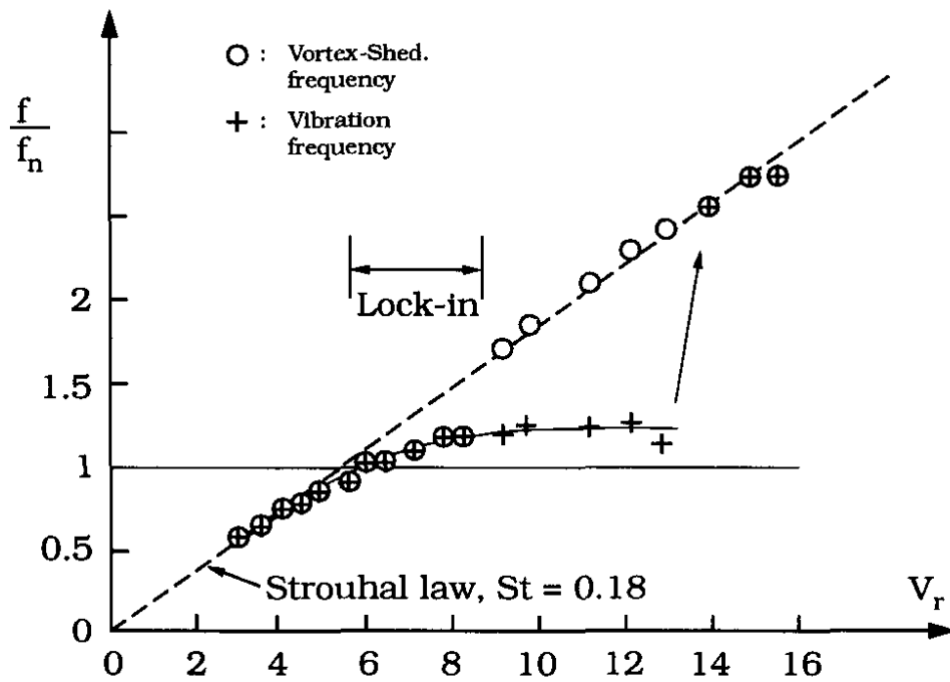
Figure 4.6 Cross-flow response of a submerged cylinder (Sumer and Fredsøe, 2006)

The VIV phenomenon is self-limiting (Figure 4.7) because of the balance between the hydrodynamic forces and the damping. At the beginning increasing the reduced velocity U_r provides the positive energy transfer to the structure, until the energy balance is reached in the lock-in region and A_{max}/D is obtained. Further the oscillation frequency f_{osc} desynchronizes with the natural frequency f_n and lock-in is destroyed.
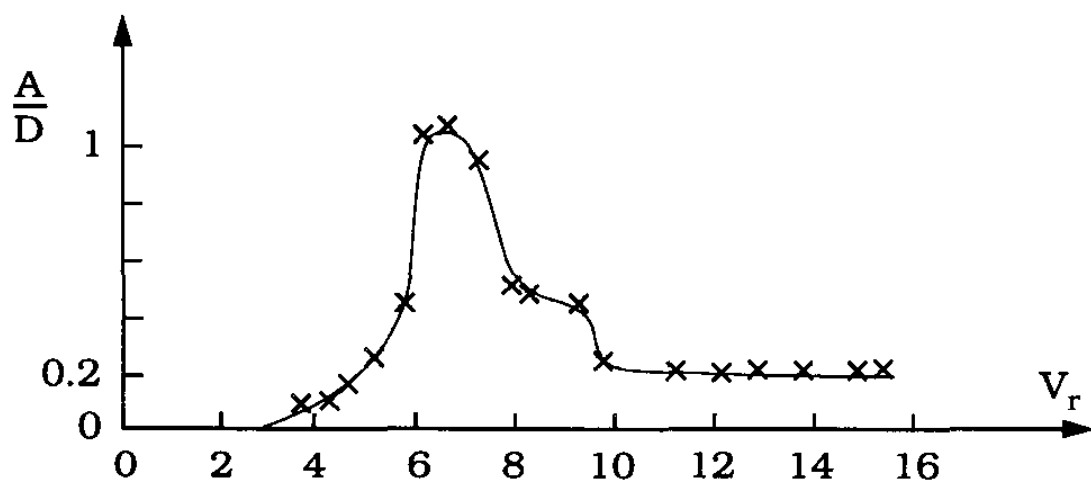
Figure 4.7 Dependency between A/D and Ur in the case of submerged circular cylinder (Sumer and Fredsøe, 2006)

32

4.1.7 Effect of Wall Proximity

When a pipeline is located on the seabed, it often has free spans which influence the vortex shedding distribution. According to Sumer and Fredsøe (2006), there is a number of changes that appear when a cylinder is placed near a wall:

1. If the gap-ratio $e/D \leq 0.3$ (e is the distance between the cylinder and the wall), then the vortex shedding is suppressed.

2. Moreover, the stagnation point moves to a lower angular position as the pressure distribution is not symmetric (Figure 4.8). In this case the non-zero mean lift force exists.

The separation point changes its angular position (Figure 4.9), i.e. at the free-stream side it will move upstream and relocates downstream at the wall side.
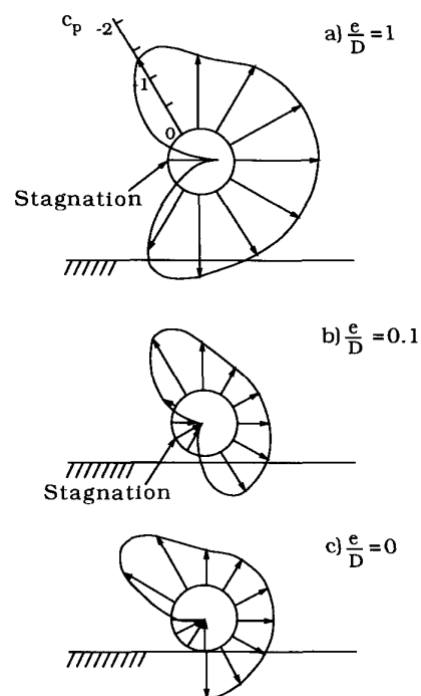
Figure 4.8 Pressure distribution on a cylinder near a wall. $C_p=(p-p0)/(0.5\rho U^2)$. (Sumer and Fredsøe, 2006)
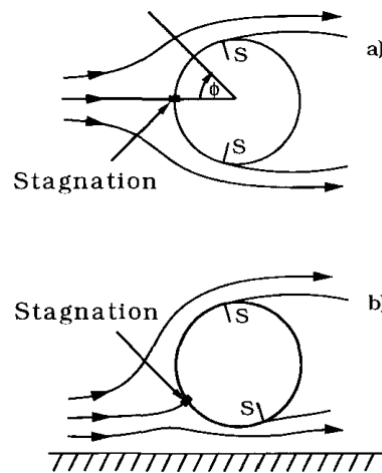
Figure 4.9 Flow around circular cylinder: a) a free cylinder, b) a near-wall cylinder (Sumer and Fredsøe, 2006)

4.1.8 Summary

The theory chapter describes the VIV phenomenon, which forces are acting and how they depend on a flow regime. Vortex-Induced Vibration is a very common phenomenon connected particularly with a circular cylinder submerged into still water. In order to summarize all the information above, a few the most important points are highlighted:

1. Vortex shedding phenomenon presents in all flow regimes for $Re > 40$. It is a result of the instability existing between two free layers formed from the separation point into downstream flow.

2. The Reynolds number affects a lot the mechanics of vortices and the boundary layer physics.

3. The oscillation frequency synchronizes with the natural frequency of the system and results in high amplitude oscillations.

4. The VIV phenomenon is self-limiting due to energy balance between the hydrodynamic forces and structural damping.

5. The mean drag force is the sum of the form drag $\overline{F_p}$ and the friction drag $\overline{F_f}$, and the drag coefficient C_D is the function of Reynolds number.

6. The gap ratio e/D greatly influences the vortex shedding distribution and may suppress it if the cylinder is placed close to a wall.

4.2 Computational Fluid Dynamics

Computational Fluid Dynamics (CFD) is a part of fluid mechanics that is dedicated to solve and analyze various systems involving fluid flow by means of numerical methods. CFD requires a huge amount of computational capacity that is why to solve complex systems of fluid interactions with surfaces defined by boundary conditions super-computers should be used. Computation Fluid Dynamics simulations are applicable for different industries particularly in marine engineering.

Despite there are various codes created to solve fluid mechanics problems, all the variants are based on the same principles and consist of three main parts: a pre-processor, a solver and a post-processor.

The pre-processing part includes the definition of investigating domain, the mesh generation, the fluid properties and the boundary conditions of the domain. Basically, the required fluid parameters (pressure, velocity and etc.) are calculated in each cell that is why the larger the number of cells, the more accurate solution is obtained. But as mentioned above, CDF simulation depends on the computational capacity, therefore, the optimal meshes are non-uniform: coarser in less important areas where changes of fluid properties are not so meaningful, and finer in areas where fluid properties change in a big scale from cell to cell.

The solver part includes the integration of all fluid flow equations over all the domain volumes, discretization of the obtained equations into an algebraic equation system, and then solution of the system of equations by means of an iterative method.

The post-processing part includes the various visualization methods of solved equations: mesh display, plots of calculated parameters at a different time step, 2D and 3D flow interaction with the investigated body.

4.2.1 OpenFOAM

OpenFOAM is an open source CFD software that is written in C++ programming language. It does not have visualization desktop, in order to set up a simulation it is necessary to change certain files in the case directory and use the system terminal. The case directory consists of three main folders: *0* folder, *constant* and *system*. The directory *0* contains files describing initial and boundary conditions. The directory *constant* contains data about the mesh generation (surfaces, faces, points), the dynamic motion solver and the turbulence properties. The *system* directory is dedicated to describe which discretization schemes and numerical solvers have to be used.

4.2.2 Mesh Topology

The present thesis is aimed to investigate the near-wall vortex-induced vibrations of two moving cylinders. The limiting factor of this study is the minimum distance between the cylinders. As at high Reynolds number the cylinders start to oscillate at high range and the simulation is crashed due to a cell height deformation caused by interaction between the cylinders. For this purpose, the TopoSet application is used in order to investigate the certain cases. TopoSet application creates the cells' sets and allows to divide the area of moving each cylinder. In this case the dependency of a cell deformation between the cylinders is excluded that permits to analyze the VIV phenomenon of two cylinders.

4.2.3 Numerical Grid

The discrete locations at which the necessary forces are calculated are defined by the numerical grid that is a discrete representation of the simulation domain. The numerical grid divides the whole domain into the finite number of subdomains. OpenFOAM is able to process with both structured and unstructured grids.

A structured or regular grid (Figure 4.10) consists of sets of grid lines, whereas the members of a set do not cross each other. Each point of a grid has four and six neighbors in 2D and 3D, respectively. The disadvantage of such grid is the fact that it is applicable only for simple geometry domain.
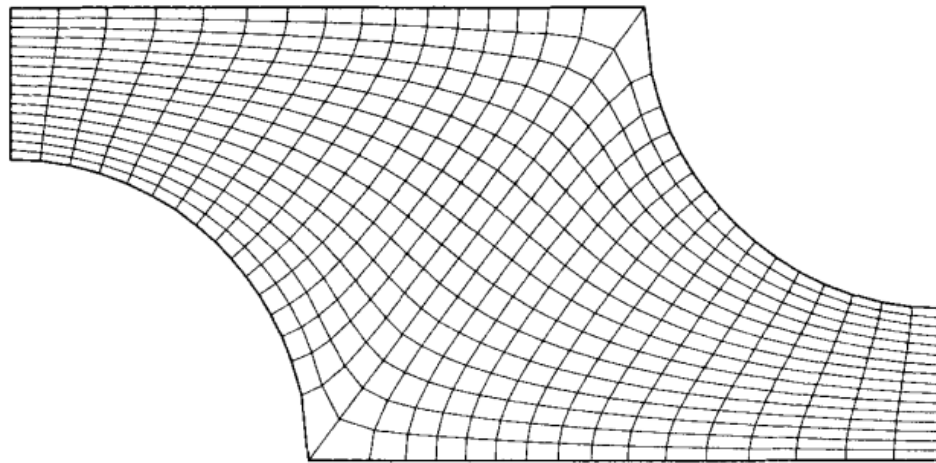
Figure 4.10 Structured grid (Ferziger and Perić, 2002)

An unstructured grid (Figure 4.11) differs from a structed grid in the fact that members of a grid family may cross each other. The elements or volumes may have any shape and the number of neighbors is not restricted. This type of grid is used for complex geometries and the solvers are generally slower than for structured grid as the system of algebraic equations is more complex. The unstructured grid is basically used with finite volume method. The grid structure is generated automatically and the compute codes are more flexible.
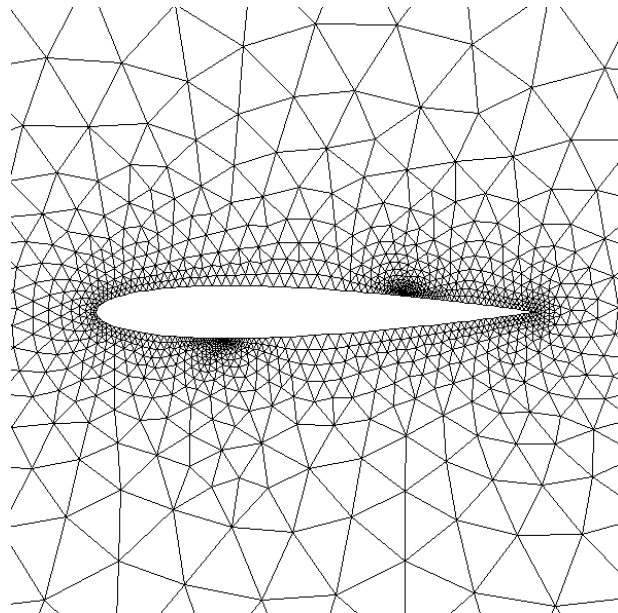
Figure 4.11 Unstructured grid [12]

4.2.4 $k - \omega$ SST Model

The present work is based on the $k - \omega$ shear stress transport (SST) turbulence model created by Menter (1994). This model is a combination of Wilcox's $k - \omega$ model and $k - \epsilon$ model. The transport equations are denoted as:

$$\frac{D\rho k}{Dt} = \tau_{ij}\frac{\partial u_i}{\partial x_j} - \beta^*\rho\omega k + \frac{\partial}{\partial x_j}\left[(\mu + \sigma_k\mu_t)\frac{\partial k}{\partial x_j}\right] \tag{4.11}$$

$$\frac{D\rho\omega}{Dt} = \frac{\gamma}{\nu_t}\tau_{ij}\frac{\partial u_i}{\partial x_j} - \beta\rho\omega^2 + \frac{\partial}{\partial x_j}\left[(\mu + \sigma_\omega\mu_t)\frac{\partial \omega}{\partial x_j}\right]$$
$$+ 2(1 - F_1)\rho\sigma_{\omega 2}\frac{1}{\omega}\frac{\partial k}{\partial x_j}\frac{\partial \omega}{\partial x_j} \tag{4.12}$$

The constants of the Wilcox's model, the $k - \epsilon$ model and the $k - \omega$ SST are shown in Table 4.1.

Table 4.1 Constants used in different turbulence models

	σ_k	σ_ω	β	β^*	γ
$k - \omega$	0.5	0.5	0.0750	0.09	$\frac{\beta}{\beta^*} - \sigma_\omega k^2/\sqrt{\beta^*}$
$k - \epsilon$	1.0	0.856	0.0828	0.09	$\frac{\beta}{\beta^*} - \sigma_\omega k^2/\sqrt{\beta^*}$
$k - \omega$ SST	0.85	0.5	0.0750	0.09	$\frac{\beta}{\beta^*} - \sigma_\omega k^2/\sqrt{\beta^*}$

The eddy viscosity ν_t is defined as:

$$\nu_t = \frac{a_1 k}{\max(a_1\omega; \Omega F_2)} \tag{4.13}$$

where $a_1 = 0.31$, Ω is the vorticity absolute value.

4.3 Near-Wall Vortex-Induced Vibrations – a Single Cylinder

4.3.1 Model Description

The model used for investigation VIV of a single cylinder is shown in Figure 4.12. The mesh domain has a rectangular shape with the boundary dimensions (defined in terms of cylinder diameter D) as $40D \times 20D$. The whole mesh domain is developed using a structures hexahedral mesh. The cylinder center is located above the bottom wall at a distance $1.5D$. The gap ratio is $e/D = 1$. The inflow is set up as a logarithmic function, the boundary layer thickness δ is equal to 0.48.
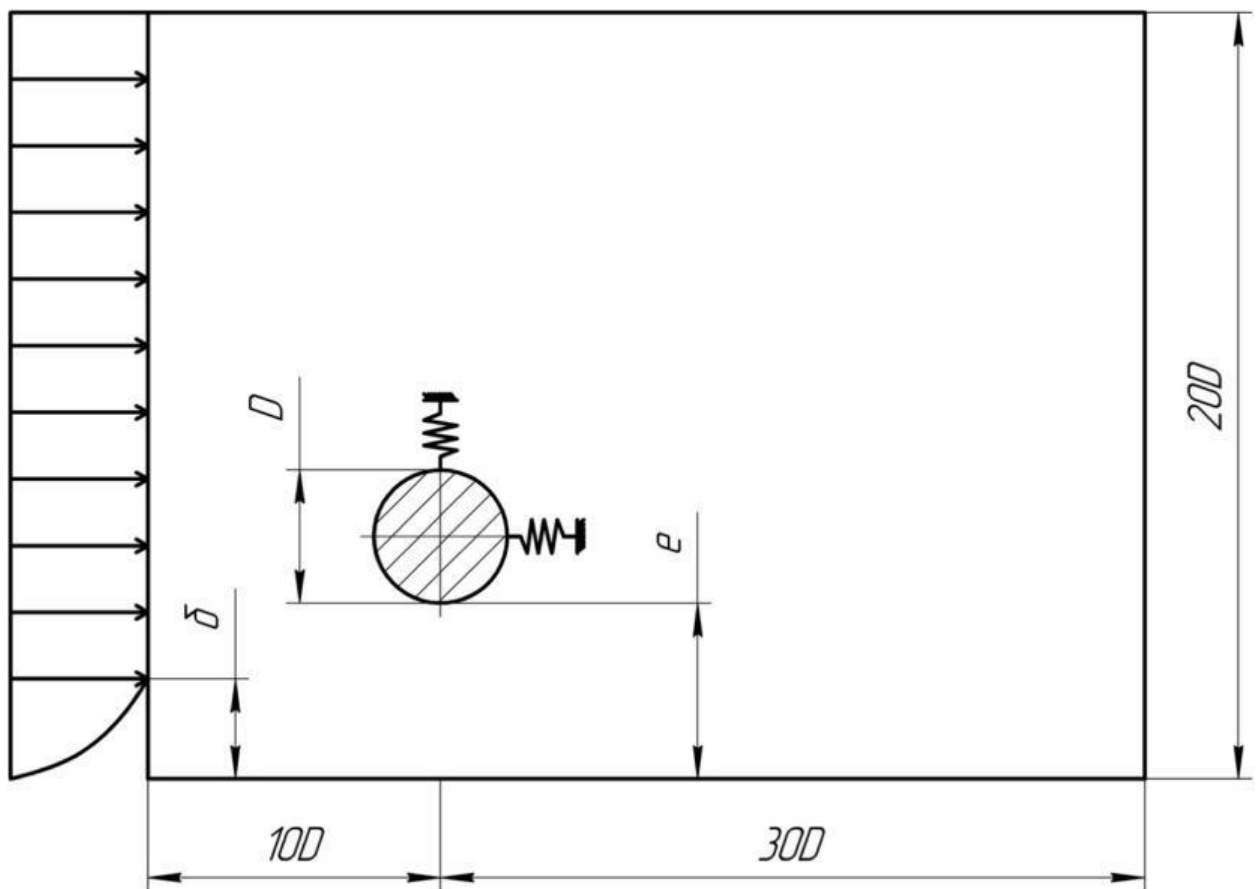

Figure 4.12 The scheme of the computational domain and the boundary conditions

The inlet flow profile is specified via the following expressions:

$$u_1(y) = \min\left[\frac{u_*}{k}\ln\left(\frac{y}{z_w}\right), U_\infty\right] \tag{4.14}$$

$$k(y) = \max\left[C_\mu^{-\frac{1}{2}}\left(1 - \frac{y}{\delta}\right)^2 u_*^2, 0.0001 U_\infty^2\right] \tag{4.15}$$

$$\omega(y) = \frac{k(y)^{1/2}}{\beta^{1/4} \, l(y)} \qquad (4.16)$$

$$l(y) = \min\left[ky\left(1 + 3.5\frac{y}{\delta}\right)^{-1}, C_\mu \delta \right] \qquad (4.17)$$

$$u_* = \frac{kU_\infty}{\ln\left(\frac{\delta}{z_w}\right)} \qquad (4.18)$$

where l is the turbulent length scale, $k = 0.41$ is the von Kármán constant, $z_w = 10^{-6}$ is the sea bottom roughness, $C_\mu = 0.09$ is the model constant, u_* is the friction velocity.

At the outlet $u, k \text{ and } \omega$ are set up as "zero gradient" condition.

At the bottom and cylinder a "no slip" condition is imposed.

At the top $u, k \text{ and } \omega$ are set up as "symmetry" condition meaning the normal components of the parameters are zero.

4.3.2 Convergence Study

In order to define how the mesh size and the time-step influence the simulation results the convergence study has been provided and the corresponding results are shown in this section. The mesh structure is given in Figure 4.13. The cell sizes are not equal over the domain: they are finer near the cylinder and bottom surface and coarser where the parameters change insignificantly. For investigating the near-wall VIV phenomenon of a single cylinder with 2 DoF the input data is provided in Table 4.2.

Table 4.2 Initial parameters for a single cylinder VIV investigation

Parameter	Symbol	Value	Unit
Diameter	D	1	m
Mass ratio	m^*	10	-
Reduced velocity	U_r	4	-
Inlet velocity	U_∞	3.6	m/s
Reynold number	Re	3.6×10^6	-
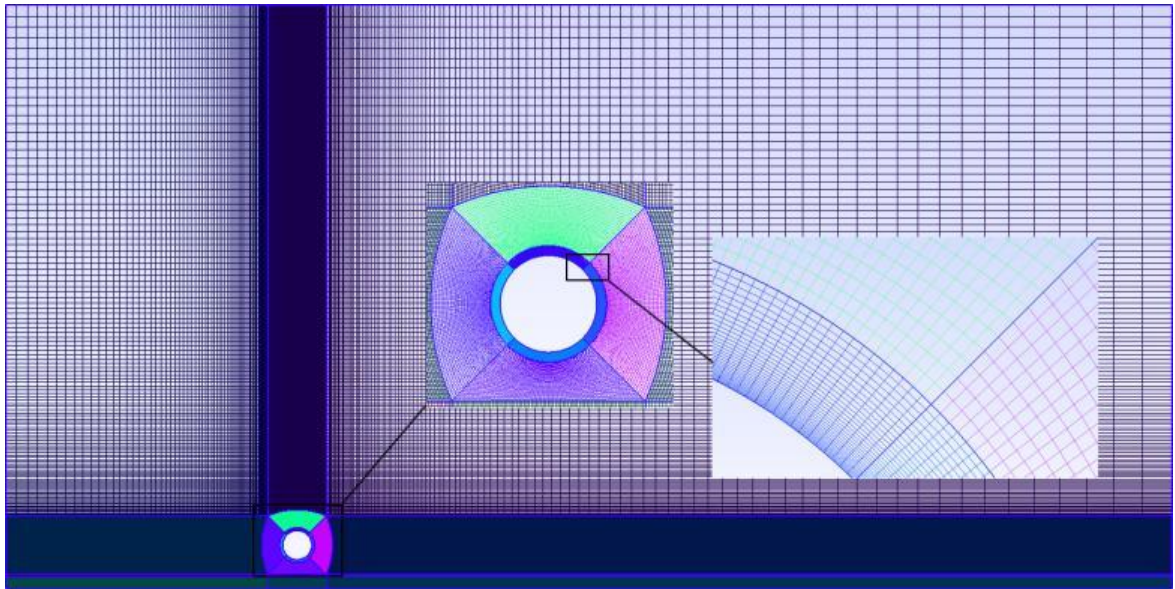
Figure 4.13 The mesh structure

To investigate how the numerical results depend on the mesh size, three meshes with different density have been generated and tested. The cell distribution of each mesh is shown in Table 4.3.

Table 4.3 Cell distribution – a single cylinder

Mesh	$y^+_{average}$	Total number of cells
A	159.72	21780
B	83.94	86720
C	60.60	124904

As the vortex-induced vibrations are generated due to drag and lift forces, the drag and lift coefficients should be used to investigate the convergence. The forceCoeffs function presented in OpenFOAM is intended to calculate the required forces for selected surfaces particularly for the cylinder. The mean value and the root-mean-square value of the corresponding coefficients are obtained as:

$$\overline{C_D} = \frac{1}{n} \sum_{i=1}^{n} C_{D,i} \tag{4.19}$$

$$\overline{C_L} = \frac{1}{n}\sum_{i=1}^{n} C_{L,i} \qquad (4.20)$$

$$C_D^{rms} = \sqrt{\frac{1}{n}\sum_{i=1}^{n}\left(C_{D,i} - \overline{C_D}\right)^2} \qquad (4.21)$$

$$C_L^{rms} = \sqrt{\frac{1}{n}\sum_{i=1}^{n}\left(C_{L,i} - \overline{C_L}\right)^2} \qquad (4.22)$$

Initially, the created meshes were simulated with the moving cylinder using pimpleDyMFoam function, but during calculating mesh C the simulation was crashed. It was decided to run simulation in the static case for the mesh density dependence evaluation. The obtained values of $\overline{C_D}$ and C_L^{rms} are presented in Table 4.4.

Table 4.4 The mesh density dependence

Mesh	$\overline{C_D}$	C_L^{rms}	Relative Error in $\overline{C_D}$	Relative Error in C_L^{rms}
A	0.7742	0.8434	43.05%	87.09%
B	0.4263	0.1039	3.42%	4.81%
C	0.4409	0.1089	0%	0%

The meshes A and B are compared with the mesh C being the reference one. The difference between the finest mesh C and the coarsest mesh A in $\overline{C_D}$ and C_L^{rms} is 43.05% and 87.09% respectively. For the mesh B and C the difference is 3.42% and 4.81% which is acceptable. In order to increase the computational efficiency, the mesh B is selected for the further simulations. The convergence plots of $\overline{C_D}$ and C_L^{rms} are shown in Figure 4.14.
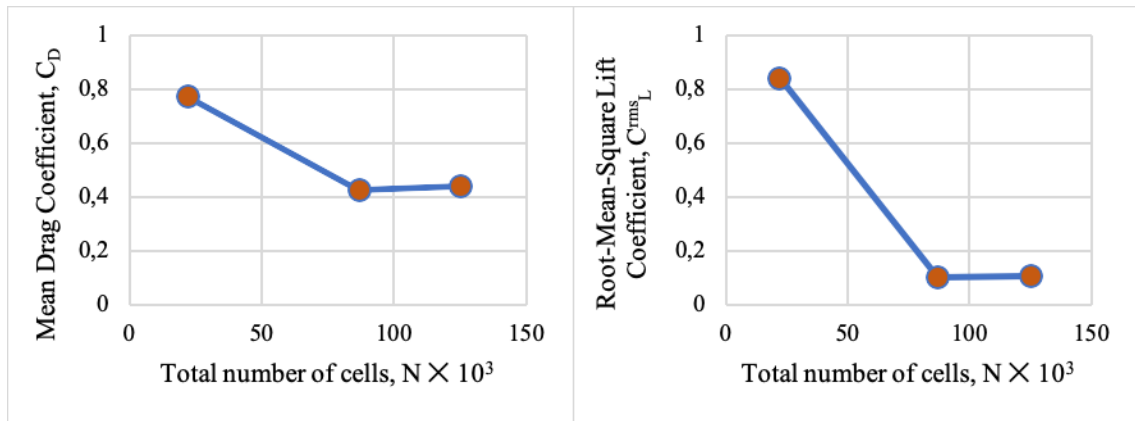
Figure 4.14 Force coefficients: mean drag (left) and root-mean-square lift (right)

Timestep dependency study is performed for the mesh B in the dynamic case. The variations of time steps are chosen based on the previously simulated dynamic case with adjustable time step. The results are shown in Table 4.5.

Table 4.5 The timestep dependency

Time step	$\overline{C_D}$	C_L^{rms}	Relative Error in $\overline{C_D}$	Relative Error in C_L^{rms}
$\Delta t = 0.0003$	1.1426	2.4554	43.05%	87.09%
$\Delta t = 0.0006$	1.1483	2.4800	3.42%	4.81%
$\Delta t = 0.0012$	1.1404	2.5051	0%	0%

Considering the computational efficiency, the time step $\Delta t = 0.0006$ is acceptable and chosen as the rational for further simulations.

4.3.3 Model Validation

The obtained results are compared with the similar experiments in the upper transition regime at $Re = 3.6 \times 10^6$. A similar study was conducted by Ong et al. (2010) using a $k - \epsilon$ model, the scope of the work was to investigate the flow around a circular cylinder close to a flat seabed at high Reynolds number. In 2003 Catalano et al. investigated a flow around a circular cylinder at $Re = 1 \times 10^6$ using URANS model. The numerical results of the investigated case are summarized in Table 4.6.

Table 4.6 Validation of the simulation: experimental data and numerical results at Re=3.6 × 10⁶

Experiment	Description	$\overline{C_D}$	C_L^{rms}	St
Present study $e/D = 1, \delta/D = 0.48$	$k - \omega\ SST\ URANS$	0.4263	0.1039	0.3263
Ong et al. (2010) $e/D = 1, \delta/D = 0.48$	$k - \epsilon\ URANS$	0.4608	0.0857	0.3052
Janocha (2017) $e/D = 1, \delta/D = 0.48$	$k - \omega\ SST\ URANS$	0.461	0.169	0.347
Catalano et al. (2003) $Re = 1 \times 10^6$	$URANS$	0.40	-	0.31

4.3.4 Summary

The model description and the convergence study are performed in this chapter. Based on the results from the sensitivity studies mesh density and time step are selected which offer a good balance of accuracy and computational efficiency. The validation of the presented numerical model is carried out via the comparison with other experimental data made previously.

4.4 Near-Wall Vortex-Induced Vibrations – Two Cylinders

4.4.1 Model Description

The model used for investigation VIV of two cylinders is shown in Figure 4.15. The mesh domain has a rectangular shape with the boundary dimensions (defined in terms of cylinder diameter D) as $40D \times 20D$. The whole mesh domain is developed using a structures hexahedral mesh. The cylinder center is located above the bottom wall at a distance $2.5D$. The gap ratio is $e/D = 2$. The inflow is set up as a logarithmic function, the boundary layer thickness δ is equal to 0.48.
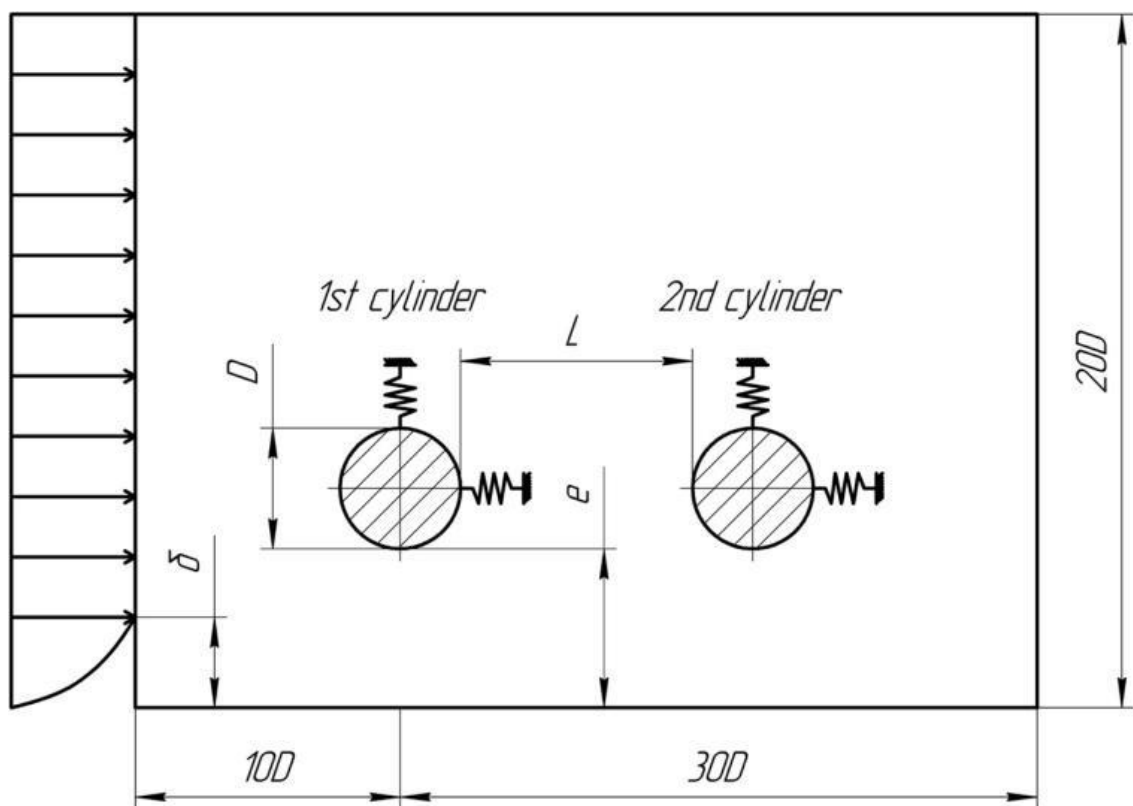

Figure 4.15 The scheme of the model of 2-DoF near-wall VIV

In the present work in order to investigate the VIV influence two cylinders with even diameter three meshes were created with different distance between the cylinders $L = 4D; 5D; 6D$, respectively. The initial parameters for simulation setup are presented in Table 4.7.

Table 4.7 Initial parameters for two cylinders VIV investigation

Parameter	Symbol	Value	Unit
Diameter	D	1	m
Mass ratio	m^*	10	-
Boundary layer thickness	δ	0.48	m
Gap ratio	$e\backslash D$	2	-
Reduced velocity	U_r	4	-
Inlet velocity	U_∞	3.6	m/s
Reynold number	Re	3.6×10^6	-
Sea bottom roughness	z_w	1×10^{-6}	m

4.4.2 Convergence Study

This section is dedicated to investigate a grid and timestep independence. The number of cells is summarized in Table 4.8. The cells distribution is not equal throughout the mesh domain: cells are finer near the cylinders and coarser in the regions where changes of forces are not significant. The convergence study is performed for the mesh with the gap ratio $e\backslash D = 2$ and the distance between the cylinders $L = 4D$.

Table 4.8 Cell distribution – two cylinders

Mesh	$y^+_{average}$		Total number of cells
	The 1st cylinder	The 2nd cylinder	
A	76.03	69.70	46504
B	62.27	56.22	116376
C	38.42	34.44	146424

The values of the coefficients are shown in Table 4.9.

Table 4.9 The mesh density dependence

Mesh	The 1st cylinder		The 2nd cylinder	
	$\overline{C_D}$	C_L^{rms}	$\overline{C_D}$	C_L^{rms}
A	$0.4661_{(-10,16\%)}$	$0.1479_{(-29,96\%)}$	$0.3405_{(-1,36\%)}$	$0.5305_{(-27,12\%)}$
B	$0.4516_{(-6,74\%)}$	$0.1248_{(-9,66\%)}$	$0.3514_{(-4,61\%)}$	$0.4897_{(-17,34\%)}$
C	$0.4231_{(0\%)}$	$0.1138_{(0\%)}$	$0.3359_{(0\%)}$	$0.4173_{(0\%)}$

The meshes A and B are compared with the mesh C being the reference one. The difference between the finest mesh C and the coarsest mesh A in $\overline{C_D}$ and C_L^{rms} is 10.16% and 29.96% and 1.36% and 21.12%, for the first and the second cylinder respectively. For the mesh B and C the difference is 6,74% and 9,66% and 4.61% and 17.34%, for the first and the second cylinder respectively, which is acceptable. In order to increase the computational efficiency, the mesh B is selected for the further simulations. The convergence plots of $\overline{C_D}$ and C_L^{rms} are shown in Figure 4.16.
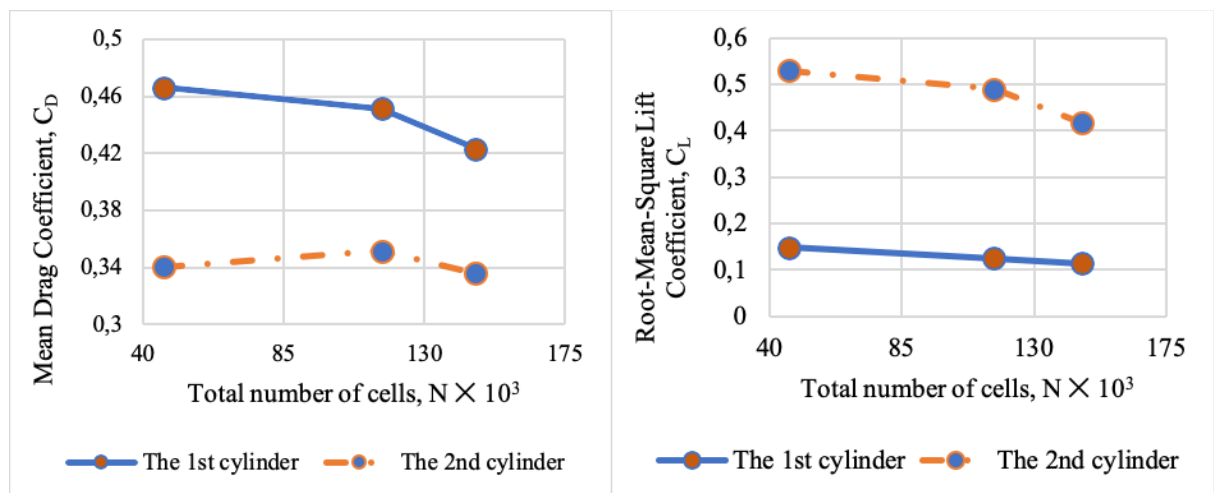

Figure 4.16 Force coefficients: mean drag (left) and root-mean-square lift (right)

The timestep study is performed for mesh B and the results are given in Table 4.10.

Table 4.10 The timestep dependence

Time step	The 1st cylinder		The 2nd cylinder	
	$\overline{C_D}$	C_L^{rms}	$\overline{C_D}$	C_L^{rms}
$\Delta t = 0.0005$	0.4514	0.1209	0.3512	0.4605
$\Delta t = 0.001$	0.4514	0.1235	0.3481	0.4725
$\Delta t = 0.002$	0.4516	0.1238	0.3477	0.4733

4.4.3 Summary

In the Chapter 4.4 pre-processing of the simulation is described as well as the convergence study. The case matrix for the further investigation is given.

4.5 Results and Discussion

The chapter 4.5 shows the obtained result of simulations in case of two cylinders with even diameters and various distance between the cylinders. The dependency of hydrodynamic forces on the distance between the cylinders is described and shown. The chapter includes the discussions about the vibration frequency of the cylinders and their motion trajectories as well.

4.5.1 Hydrodynamic Forces

For each case the mean drag coefficient $\overline{C_D}$, mean lift coefficient $\overline{C_L}$ and root-mean-square drag coefficient C_D^{rms} and root-mean-square lift coefficient C_L^{rms} are calculated (Table 4.11) and plotted in dimensionless time range $\tau = tU/D = 80 - 140$ (Figure 4.17, Figure 4.18, Figure 4.19). The mean lift coefficient has non-zero value due to the asymmetry of the wake in the vertical range caused by the wall presence. The decreasing of the drag coefficient of the second cylinder is caused by shielding effect. The vorticities of the first cylinder create low pressure in the wake and it further contributes lowering the drag coefficient. With increasing the distance between the cylinders, the shielding effect decreases that leads to the higher drag coefficient of the second cylinder.

Table 4.11 Values of the mean drag coefficient C_D and the root-mean-square lift coefficient C_L at investigated distance between cylinders

Distance between the cylinders	The 1st cylinder				The 2nd cylinder				Difference of drag coefficients $\Delta\overline{C_D}$
	$\overline{C_D}$	C_D^{rms}	$\overline{C_L}$	C_L^{rms}	$\overline{C_D}$	C_D^{rms}	$\overline{C_L}$	C_L^{rms}	
$L = 4D$	1.419	1.534	0.254	1.534	1.035	1.200	0.376	1.664	0.384
$L = 5D$	1.482	1.170	-0.006	1.473	1.234	1.031	0.029	1.422	0.248
$L = 6D$	1.410	1.143	-0.063	1.543	1.228	1.011	0.120	1.520	0.182
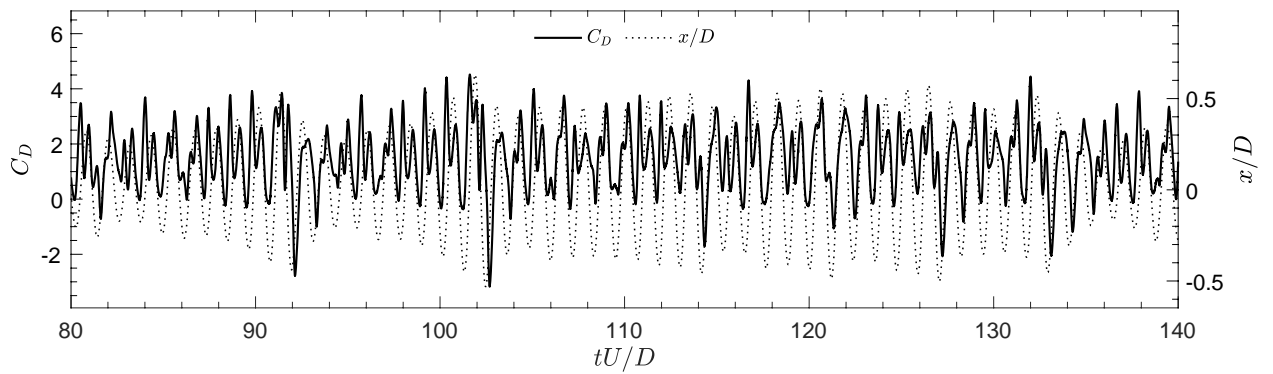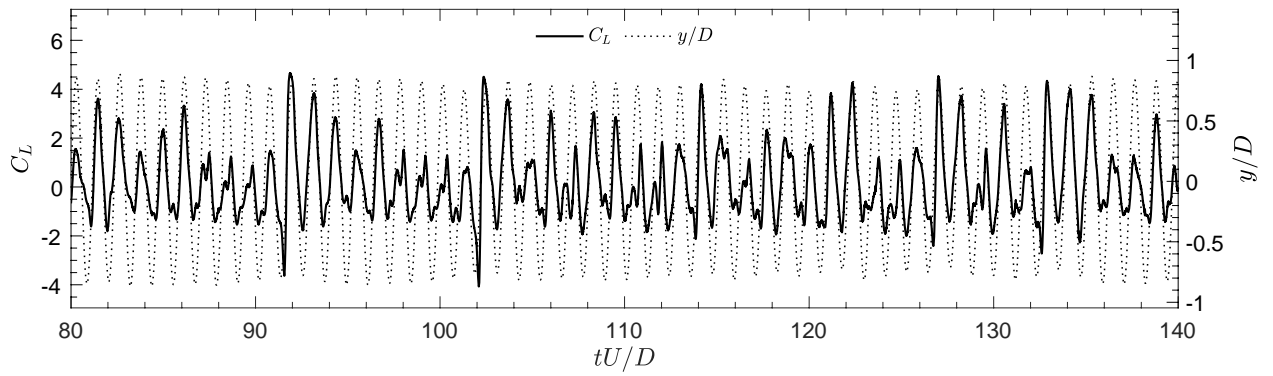
(a) the 1st cylinder
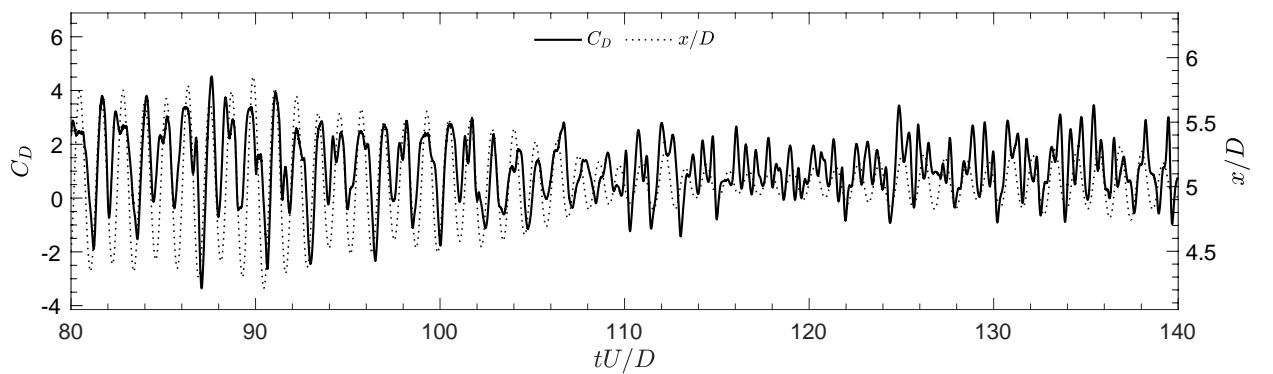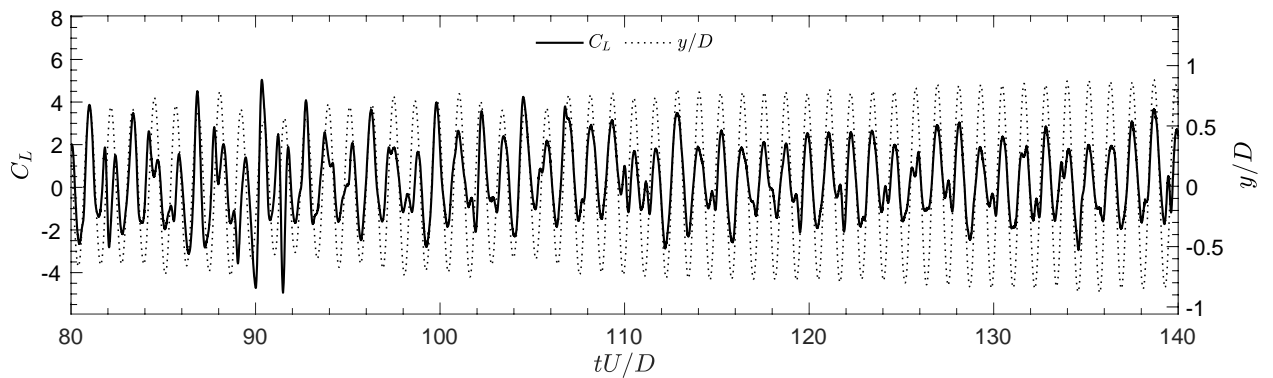
(b) the 2nd cylinder

Figure 4.17 Time histories of lift coefficient C_L, drag coefficient C_D, in-line displacement x/D and cross-flow displacement y/D at L=4D

50

(a) the 1st cylinder

(b) the 2nd cylinder

Figure 4.18 Time histories of lift coefficient C_L, drag coefficient C_D, in-line displacement x/D and cross-flow displacement y/D at L=5D
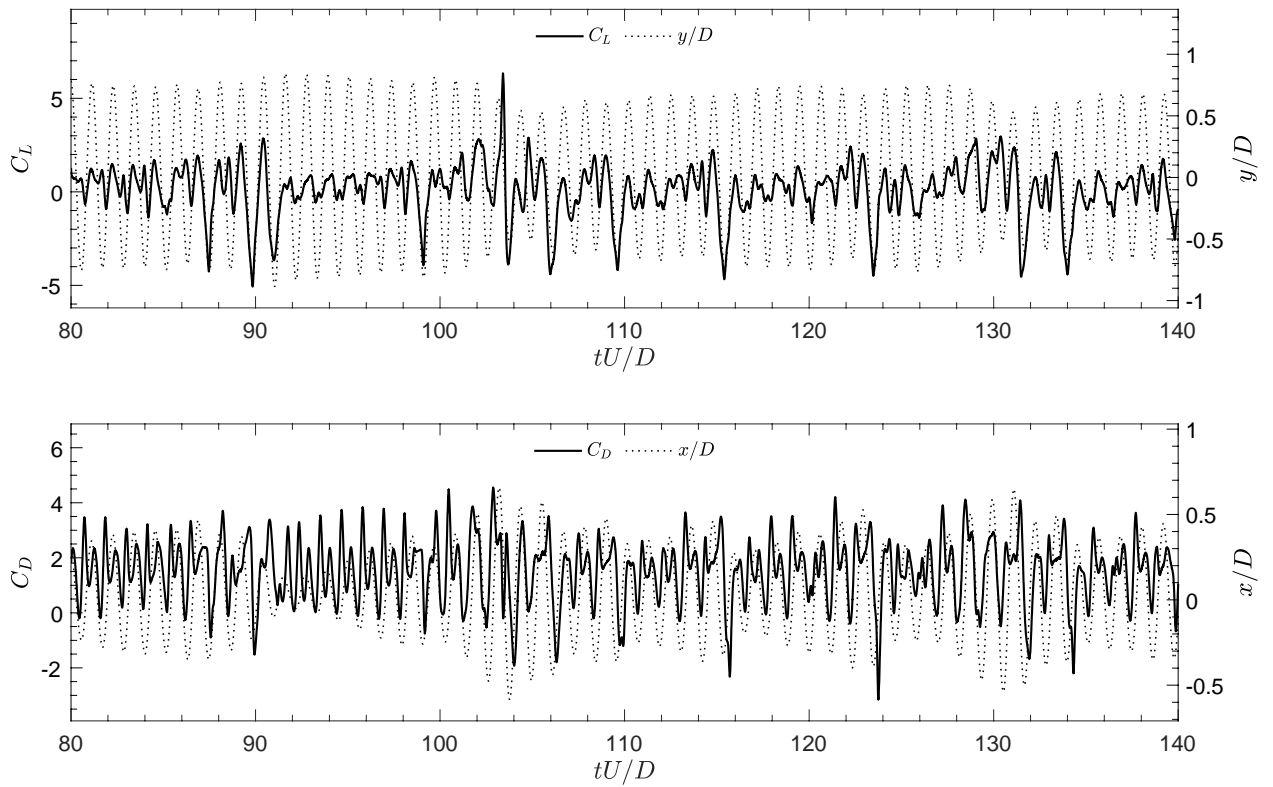
(a) the 1st cylinder
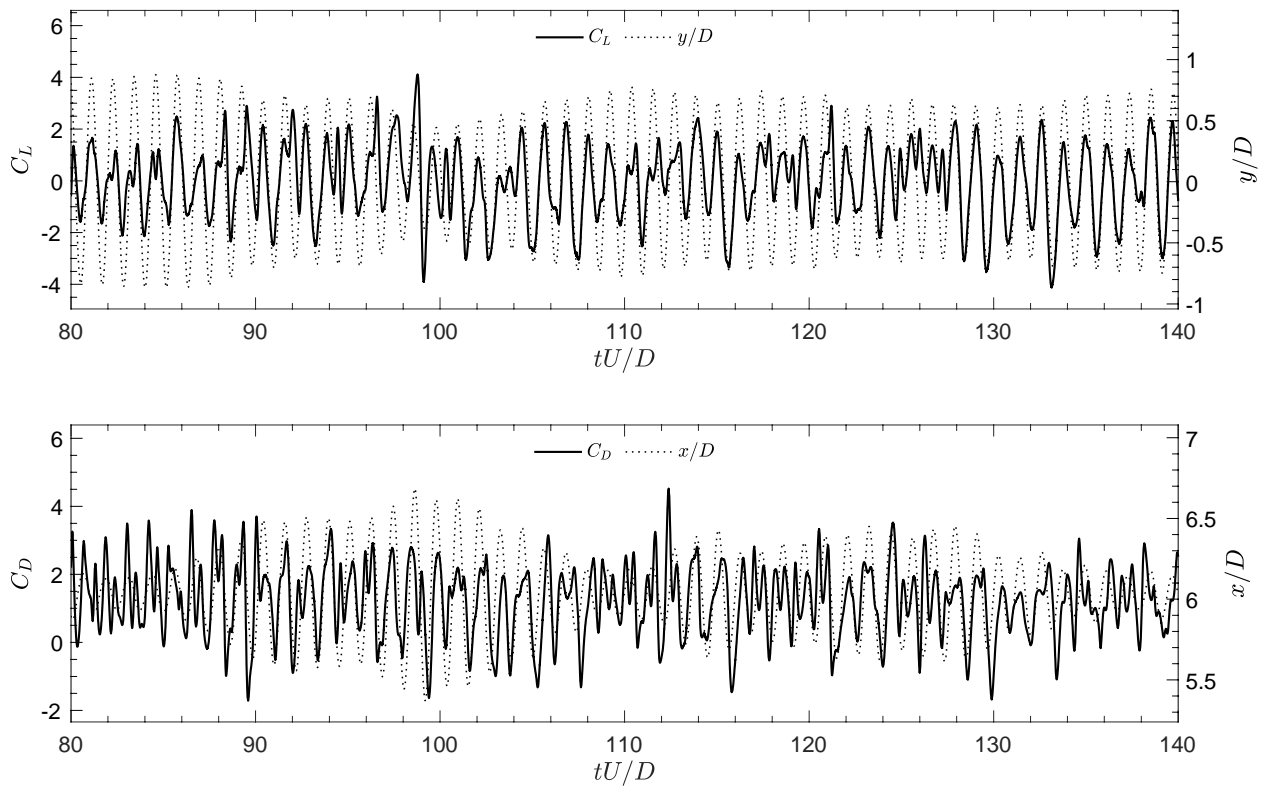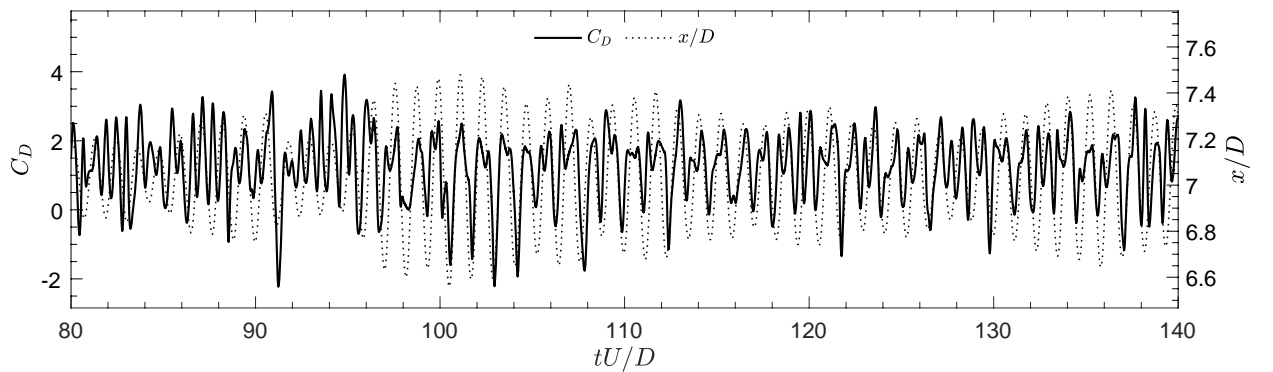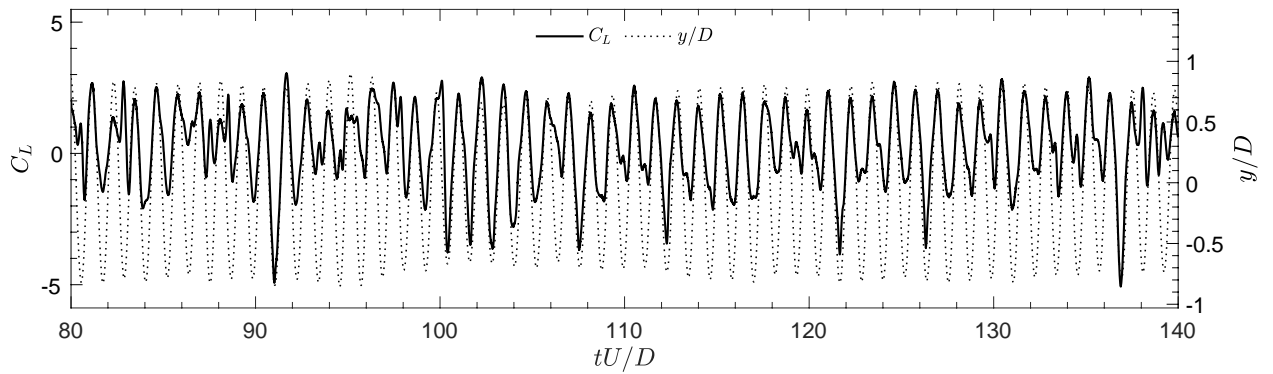

(b) the 2nd cylinder

Figure 4.19 Time histories of lift coefficient C_L, drag coefficient C_D, in-line displacement x/D and cross-flow displacement y/D at L=6D

4.5.2 Vibration Frequency

In order to compute and analyze the frequency power spectra of both the drag and lift coefficients and the in-line and cross-flow displacement the Fast Fourier Transform (FFT) is applied. The obtained results are shown in Figure 4.20, Figure 4.21 and Figure 4.22. The dominant frequencies in the in-line and cross-flow directions are coinciding and are equal approximately to 0.23. It occurs due to the vorticities from the bottom surface counteract the vorticities in the cylinder wake. Therefore, the streamwise oscillation frequency is reduced by half, which is the cause of the resonance between the transverse and streamwise vibration frequencies. The amplitude values of drag and lift forces are roughly twice as big as the amplitude values of in-line and cross-flow displacements, respectively. The lift frequency of the first cylinder has the similar value as for the second cylinder. It may occur due to the lift oscillation by means of vortices is shed from the first cylinder and collides with the second cylinder.
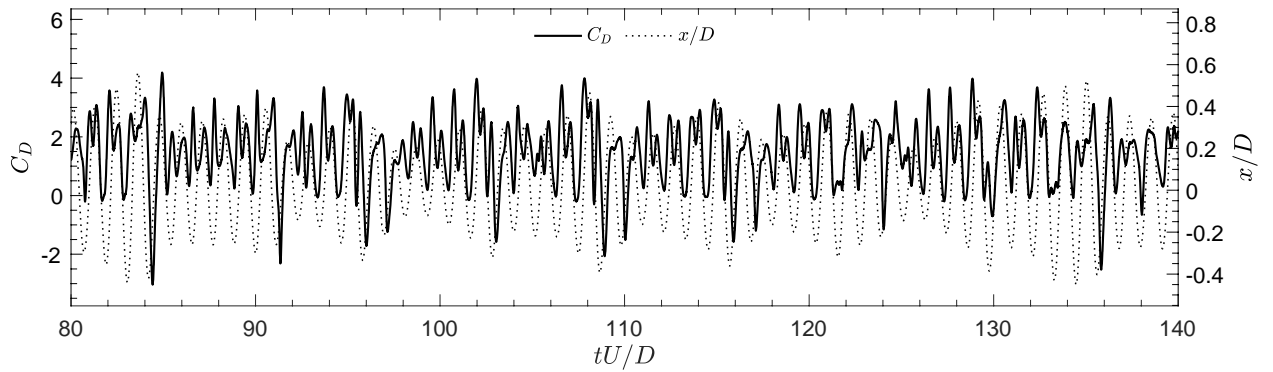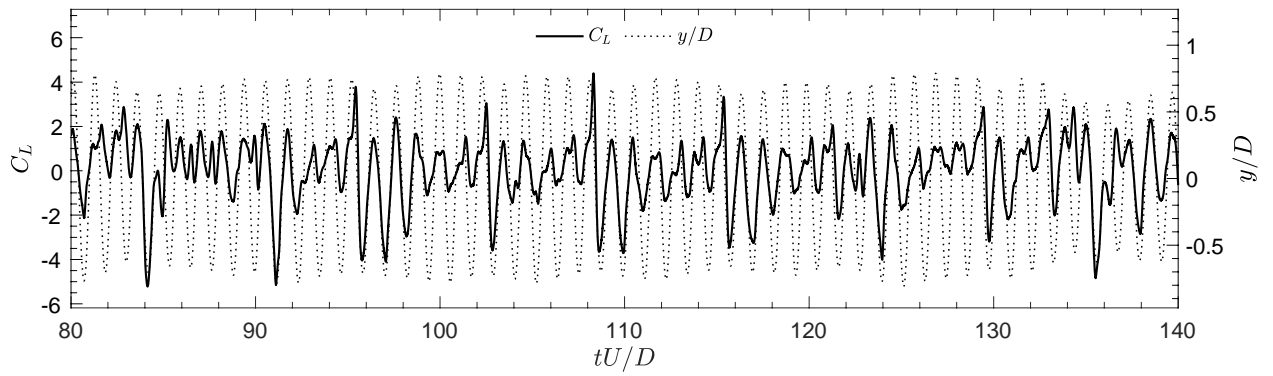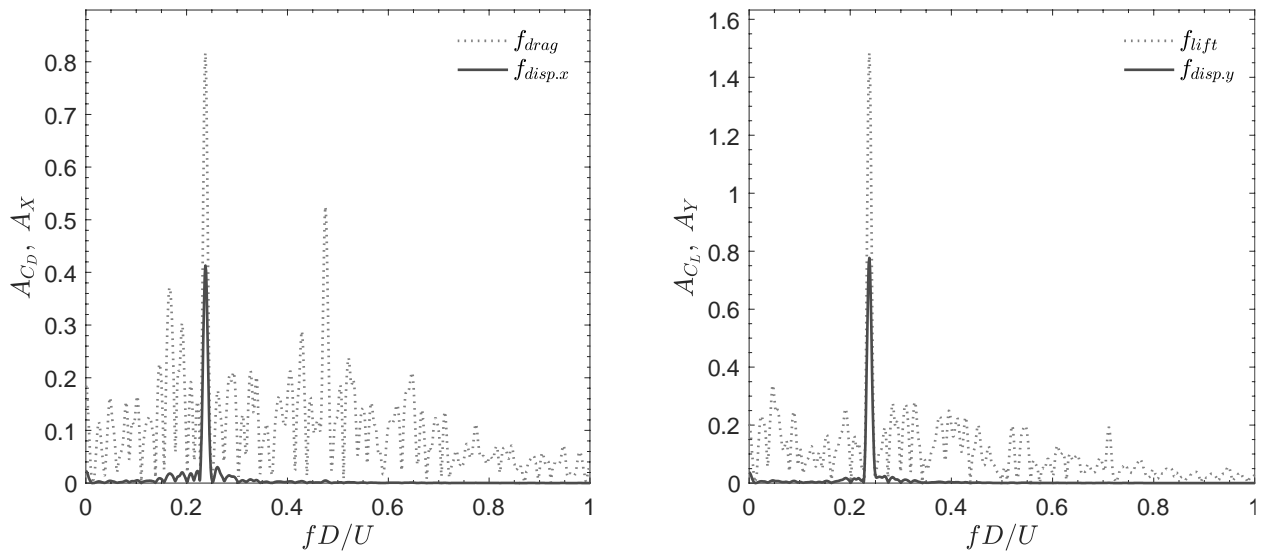
(a) the 1st cylinder
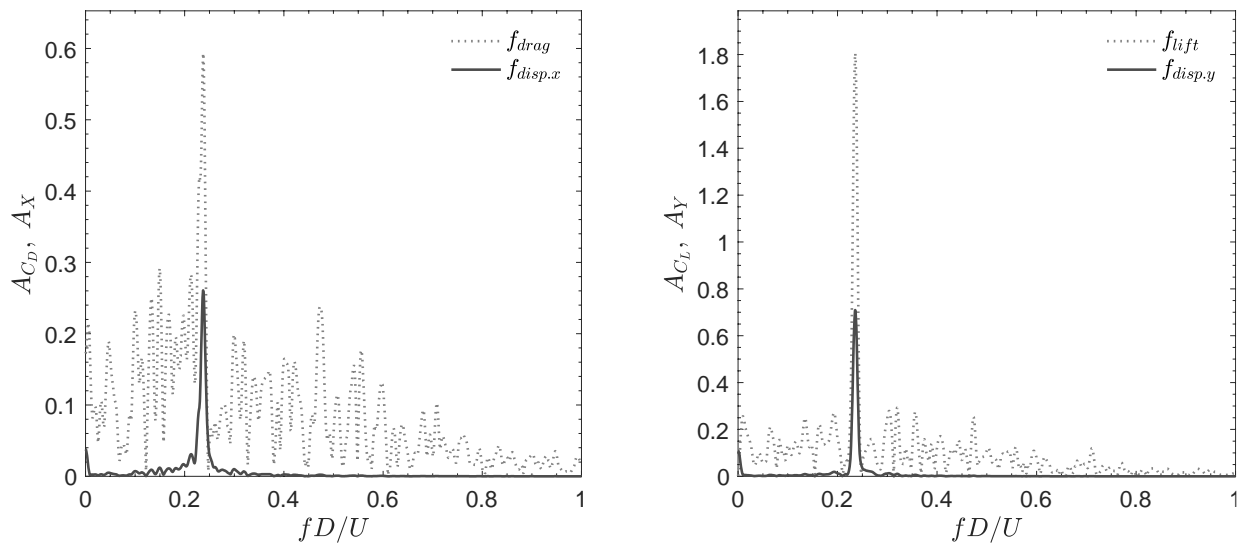
(b) the 2nd cylinder

Figure 4.20 Power spectral analysis for in-line vibration and drag (left), cross-flow vibration and lift (right) at L=4D
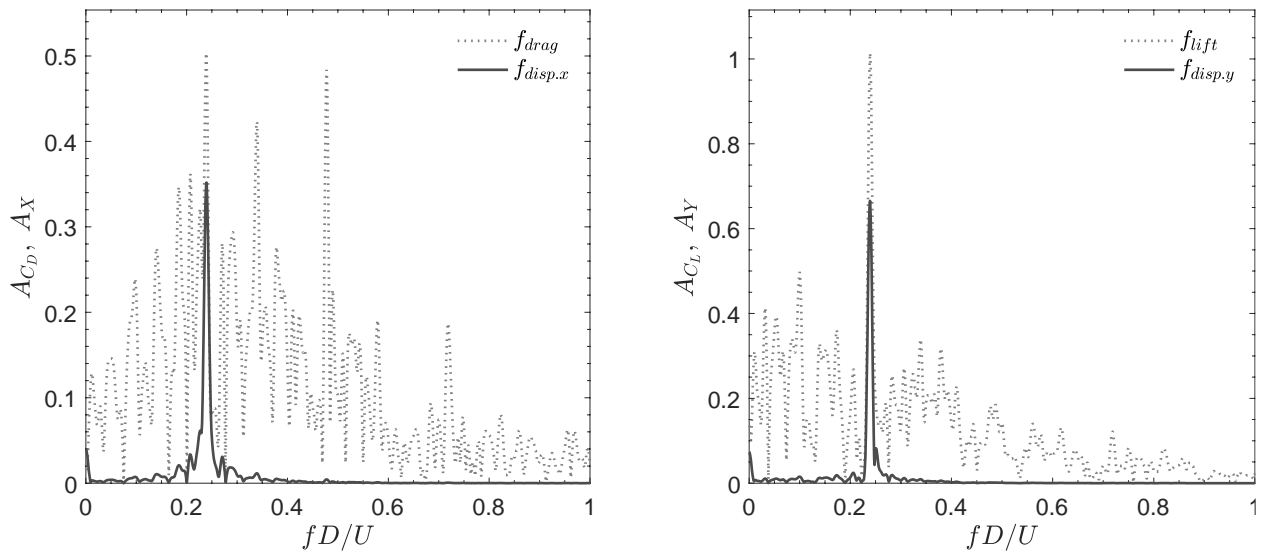
(a) the 1st cylinder
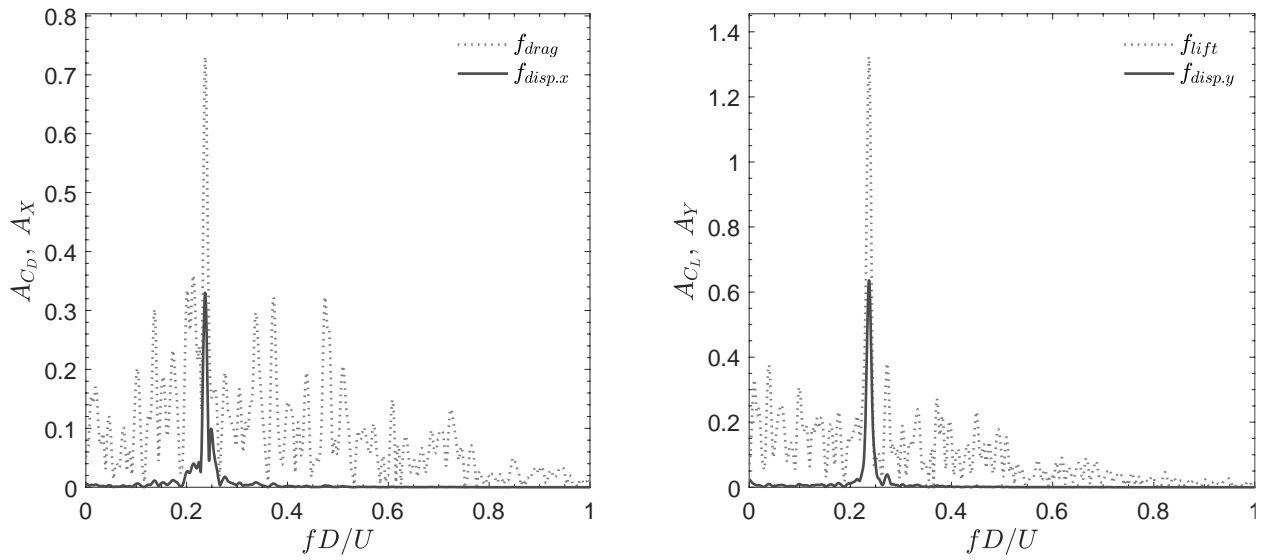
(b) the 2nd cylinder

Figure 4.21 Power spectral analysis for in-line vibration and drag (left), cross-flow vibration and lift (right) at L=5D
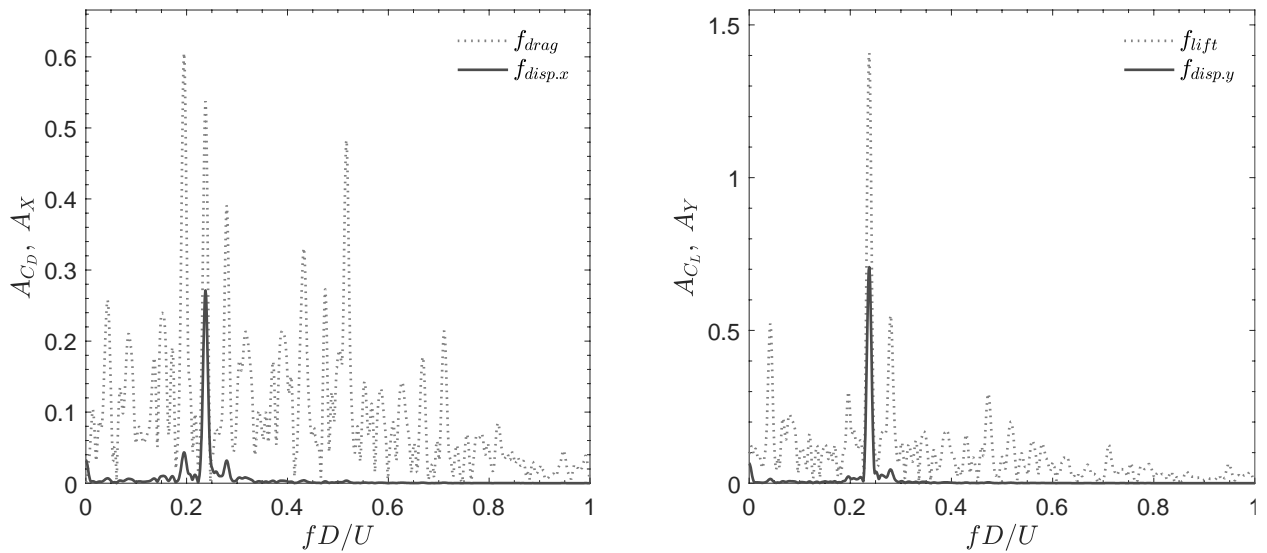
(a) the 1st cylinder
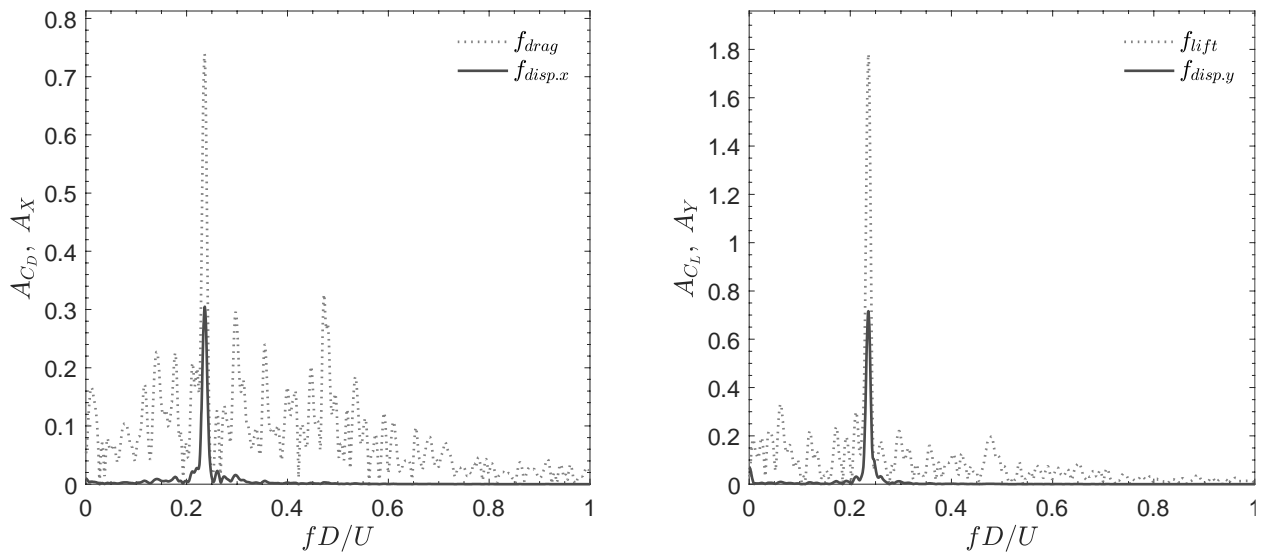
(b) the 2nd cylinder

Figure 4.22 Power spectral analysis for in-line vibration and drag (left), cross-flow vibration and lift (right) at L=6D

4.5.3 Motion Trajectory

This sub-section is dedicated to X-Y trajectories of the cylinders at investigated distances. The general shape of freely vibrating cylinder in cross-flow direction is a figure of eight. The trajectories of two cylinders at different distances are shown in Figure 4.23. The reason of the different shape of the trajectories is the proximity of the plane wall. In the free-flow case the vorticities are symmetrical in the cross-flow direction, but in the case of the wall proximity the symmetry of

vorticities is disturbed due to the wall presence. In Figure 4.23 (a) it is seen that the trajectory of the second cylinder is influenced by the vortex shedding distribution of the first cylinder. As the spacing increasing, the interaction of between the cylinders begins to decrease and the trajectory of the second cylinder starts stabilizing (Figure 4.23 (c)).

(a) *L=4D*   (b) *L=5D*   (c) *L=6D*
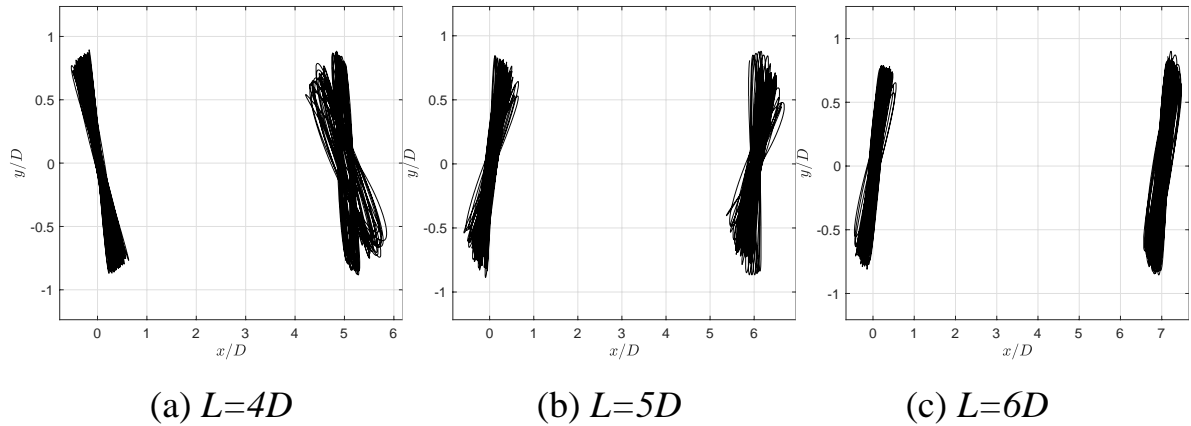
Figure 4.23 Trajectories of two cylinders for different distances L at high Reynolds number

4.5.4 Vorticity and Pressure Contours

In order to gain greater insight into the influence of the vortex shedding development in the selected cases, a visualization of vorticity and pressure contours is used for this purpose. First the mechanism of the vortex shedding is discussed based on the flow field around a single cylinder at $U_r = 4$, $\delta/D = 0.48$, $e/D = 2$ and $Re = 3.6 \times 10^6$. Figure 4.24 describes a full cycle of vortex shedding development that corresponds to 2S mode and describes the pressure distribution as well. The wake is almost symmetric, until the vorticities reach significant sizes that are affected by the bottom shear layer. The anti-clockwise vortex shed (A1) continues to grow, till the clockwise vortex shed (B1) approaches the opposite site and cuts off the dominant vortex shed from its boundary layer. After the vortex is shed and free, it is convected downstream in the wake. Then a new vortex is created and the clockwise vortex (B1) will become larger so that it will draw newly formed vortex (A2) on the opposite side. When a vortex shed reaches a significant size (D1), it forces the boundary layer to roll-up (C1).

The configuration with two even cylinders at $L = 4D$ is shown in Figure 4.25. In the case of two cylinders the vortex shedding mode corresponds to 2P mode. It means that two vortices (A1 and B1) are shed from each side during one cycle. The proximity of the horizontal wall and the vortex shedding of the first cylinder significantly affect the vortex shedding of the second cylinder by totally breaking the symmetry of the wake. Both clockwise and anti-clockwise vorticities (A2 and B2, respectively) are interacting with the second cylinder resulting in a disturbance of the vortex shedding mechanism. The vorticities create lower pressure around the second cylinder, that leads to the decreasing the drag coefficient. The anti-clockwise vortex from the bottom surface of the second cylinder (A3) forces the boundary layer to roll-up (C1). Figure 4.26 and Figure 4.27 show the vortex shedding development mechanism and the pressure distribution at $L = 5D$ and $L = 6D$, respectively. The situations are similar to that of the two cylinders at $L = 4D$. The diversity is contained in the pressure difference decreasing around the second cylinder during increasing the distance between the cylinders.
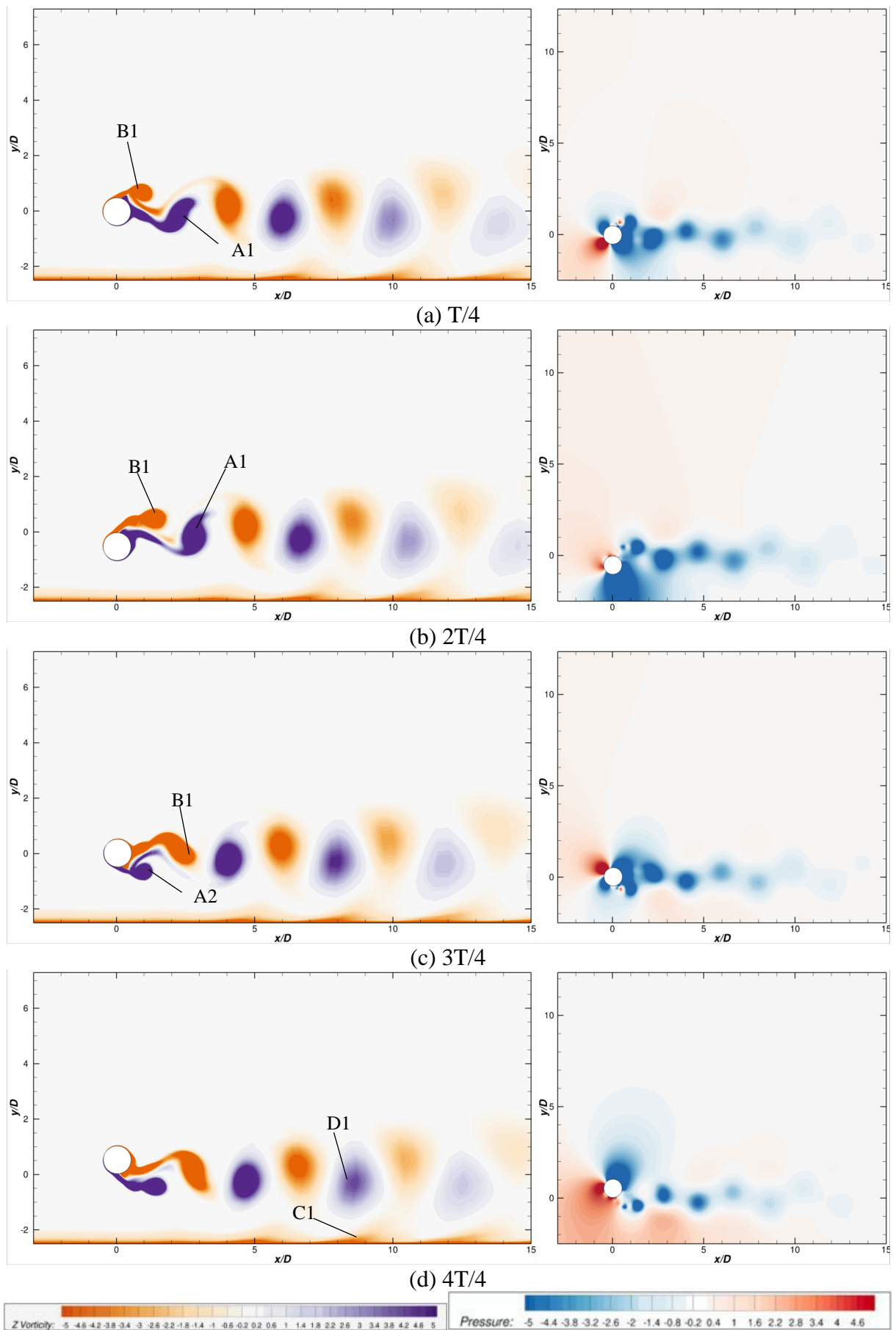
Figure 4.24 Vorticity contour (left) and pressure contour (right) of a single cylinder at Ur=4, Re=3.6x10⁶

59
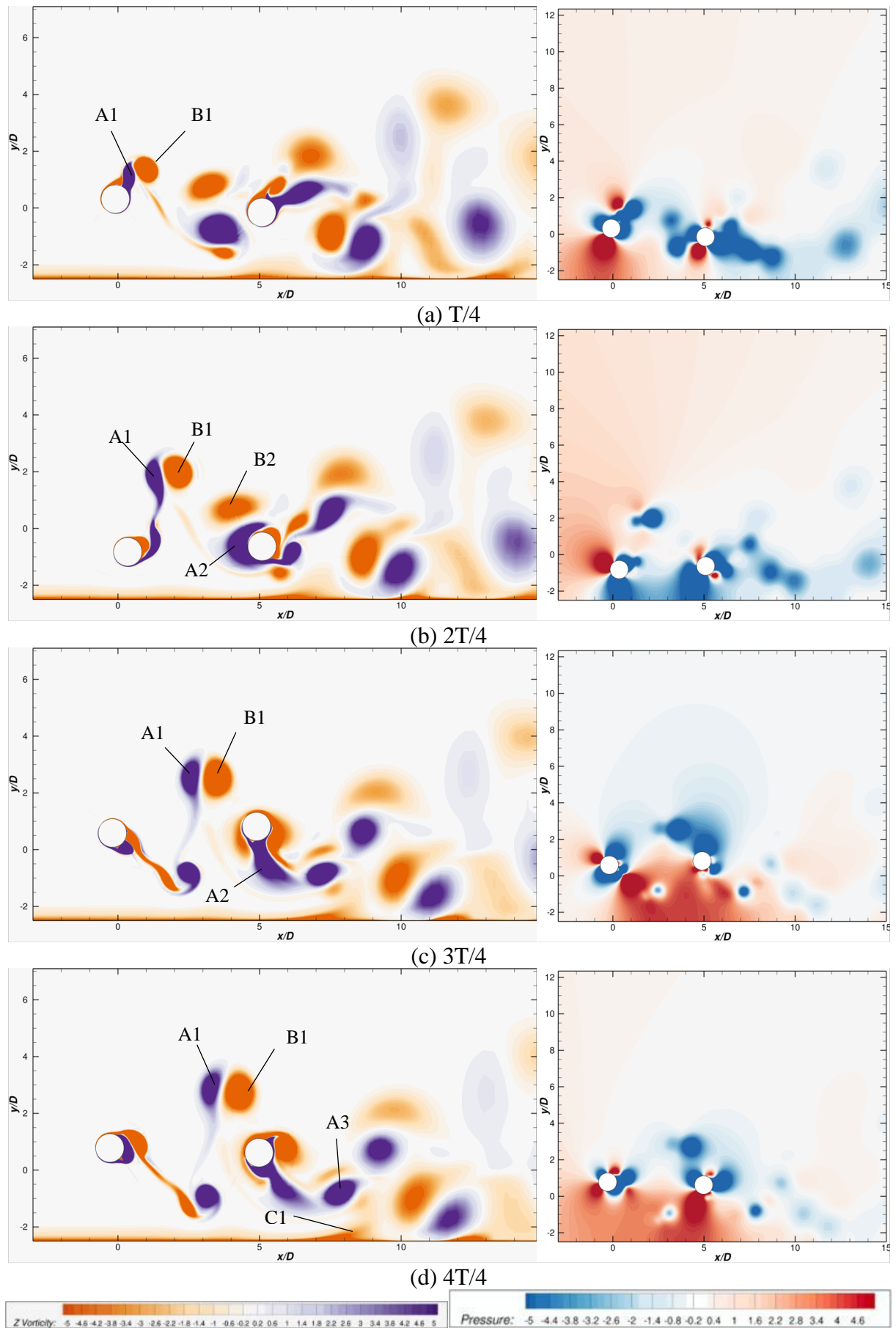
Figure 4.25 Vorticity contour (left) and pressure contour (right) of two cylinders at L=4D

(a) T/4

(b) 2T/4

(c) 3T/4

(d) 4T/4

Z Vorticity: -5 -4.6 -4.2 -3.8 -3.4 -3 -2.6 -2.2 -1.8 -1.4 -1 -0.6 -0.2 0.2 0.6 1 1.4 1.8 2.2 2.6 3 3.4 3.8 4.2 4.6 5

Pressure: -5 -4.4 -3.8 -3.2 -2.6 -2 -1.4 -0.8 -0.2 0.4 1 1.6 2.2 2.8 3.4 4 4.6
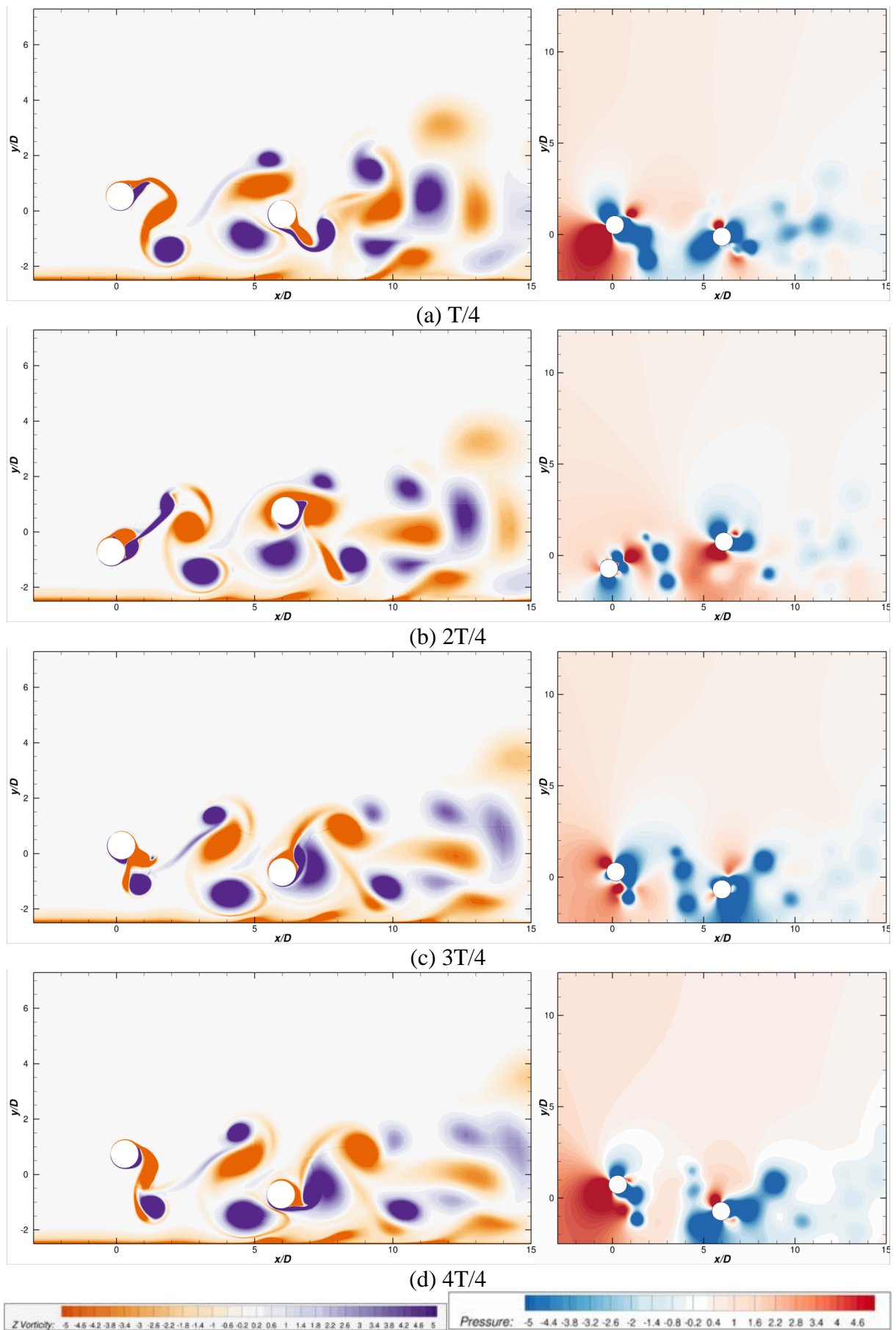
Figure 4.26 Vorticity contour (left) and pressure contour (right) of two cylinders at L=5D
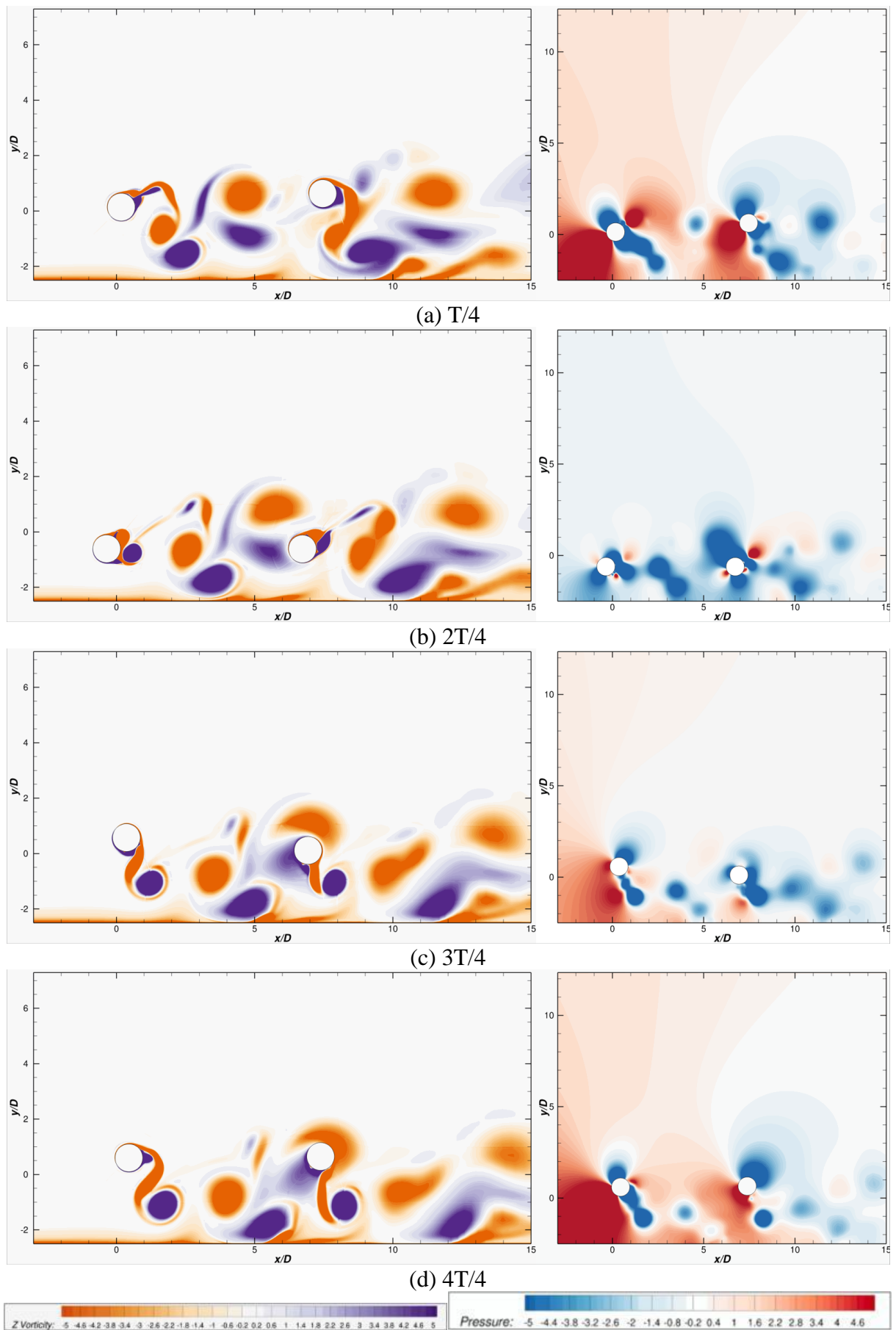
Figure 4.27 Vorticity contour (left) and pressure contour (right) of two cylinders at L=6D

4.6 Summary

Based on the present study the following conclusions can be formed:

- The wall proximity magnifies the mean lift force, while the mean drag force remains approximately with the same value.

- The vorticities from the bottom surface disturb the symmetry in the wake of a cylinder, therefore, the oscillation frequency in the in-line direction is reduced by half. This factor is the reason of the resonance of both streamwise and transverse oscillation frequencies.

- As the distance between the cylinders decreases, the vortex shedding of the first cylinder induces the deviation of the trajectory of the second cylinder from its normal shape.

- The drag force is less in the second cylinder, as the vortex shedding causes the shielding effect: the flow velocity decreases due to the interaction with the first cylinder and, moreover, the vorticities of the first cylinder create lower pressure in the wake instigating the decreasing the value of the drag force of the second cylinder.

5 PIPELINE ON-BOTTOM PROTECTION

The chapters above show that in order to maintain pipeline operational integrity as long as it is possible, it is necessary to implement various methods of the offshore pipeline protection. This chapter is dedicated to pipeline on-bottom protection methods and to the environmental assessment of a pipeline protection.

5.1 Protection against Ice Gouging

An ice ridge may exert considerable loads during ice gouging and designing a pipeline that is possible to withstand these loads is considered to be inefficient. In this case there are three main options to protect a pipeline (Figure 5.1):

- Ice management. This method includes towing ice features that can damage the structure potentially by means of changing their direction. For this purpose, one or two towing vessels are used.

- Shielding. This method consists in a construction of a protective structure that is able to take the load from an ice feature and keep the equipment undamaged. This method is effective for local installations, such as well heads, manifolds, production trees. For a pipeline that is stretching for a few kilometers the certain option would be inefficient.

- Trenching and burial. Seabed trenching is considered to be the most commonly used method for a pipeline protection. Besides a protection against ice gouging, it offers some advantages such as thermal insulation, free span elimination, reduction of hydrodynamic forces from waves and currents.
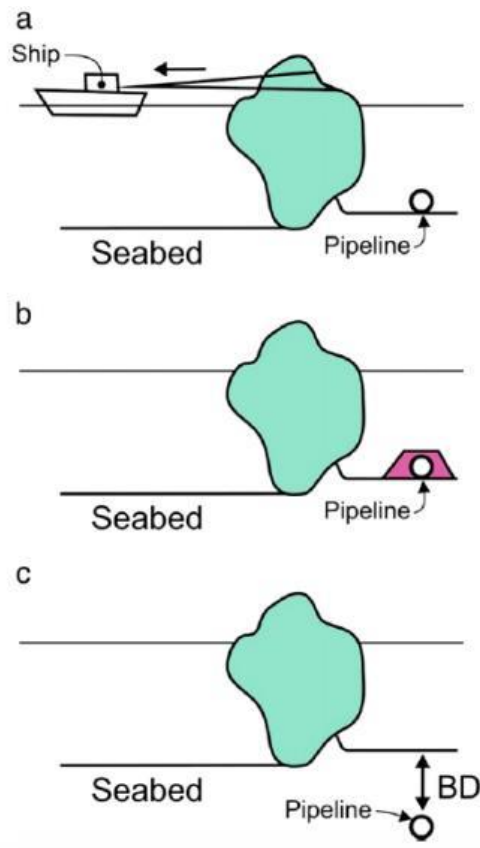
Figure 5.1 Methods of a pipeline protection against ice ridges: a) ice management; b) shielding; c) trenching and burial (BD-burial depth). (Barrette, 2011)

5.1.1 Methods of Pipeline Trenching

As it was mentioned above, a pipeline has to be buried sufficiently beneath the ice keel. Figure 5.2 shows the possible zones of the pipeline installation.

- Zone 1 corresponds to layer where soil that is scoured by an ice feature.
- Zone 2 corresponds to layer where soil is deformed below the gouge.
- Zone 3 corresponds to layer where only elastic deformation of soil occurs.
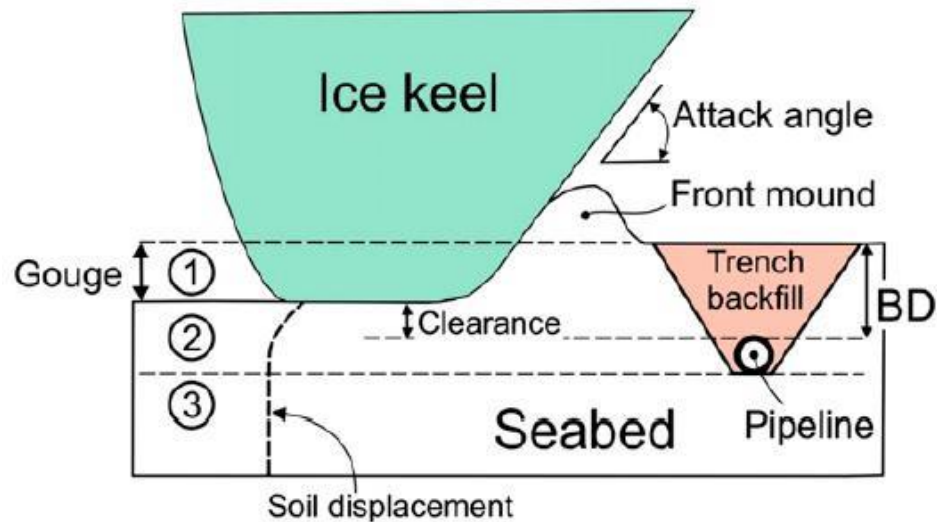
Figure 5.2 Scheme of the interaction between an ice ridge with the seabed (Barrette, 2011)

Trenching techniques is divided into pre-lay (before a pipeline is installed) and post-lay installation. The following methods are the most commonly used:

- Conventional excavation;
- Ploughing;
- Mechanical trenching;
- Hydraulic dredging.

Conventional excavation method refers to using clamshell bucket dredges, hydraulic backhoes or similar equipment in shallow waters. It is proven method but time-consuming and can be applied both in summer and winter periods.

Ploughing method is usually implemented for post-lay pipeline installation and allows to trench a long pipeline route due to relatively quick advance rate. According to Paulin et al. (2013), ploughing is capable to achieve a trench depth of 2.5m if soil is soft enough.

Mechanical trenching method is typically used for burying umbilicals and cables. There are two main types of trenchers: barge-mounted trenchers and crawler style trenchers. The first one can be implemented in water depth less than 100m, while the second one allows operating in water depths up to 1500m.

Hydraulic dredging method uses two main hydraulic dredgers for trenching purpose: trailing suction hopper dredgers (TSHD) and cutter suction dredgers (CSD). The TSHD approach consists in lowering the suction head to the seabed and pumping soil into the hopper. In order to empty the hopper, the vessel goes to special areas or smaller vessels may be used for disposal. As the suction pipe is flexible, it is difficult to control its position. In this case it results in a wide trench. The CSD approach consists in using a rotating cutter head that breaks the soil. During breaking the soil, slurry is pumped through the discharge pipe and is accumulated in a few hundred meters away to a disposal area.

5.2 Protection against VIV

From time to time a pipeline location may change due to various factors such as seabed roughness, soil type, pipeline tension, its submerged weight. In this case a pipeline tends to form spans along the route that may disturb the pipeline integrity. Pipeline spans can be both single and multiple (Figure 5.3).

(a) Single span

(b) Multiple span
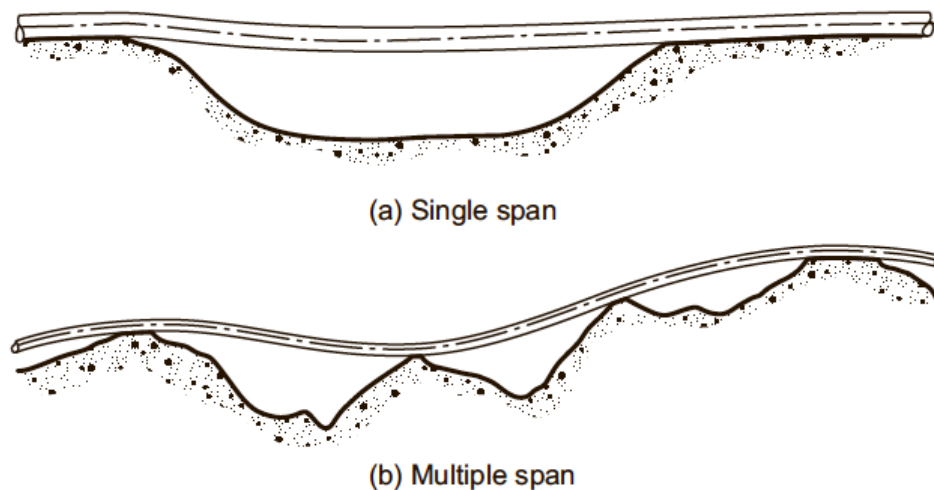
Figure 5.3 Types of free spans (Bai and Bai, 2014)

5.2.1 Span Correction Methods

Free spans along a pipeline are potentially dangerous zones as they may cause static stress increase, vortex-induced vibrations, bar buckling and fatigue damage. Nowadays, various methods for span mitigation exist such as:

- Mattresses and bags;

- Trenching;

- Rock dumping;

- Mechanical supports.

Mattresses and sand or grout bags are widespread method for span rectification in shallow waters. For deep water this method is inefficient because it is difficult to place mattresses and bags accurately and it requires a lot of time. Generally, the certain method is used for rectification of a few spans, if there are a lot of spans along the pipeline route, it becomes economically inefficient.

Pipeline trenching is discussed in Chapter 5.1 in more detail. This type of span mitigation has a limitation in water depth. As vortex-induced vibrations occur usually in deep waters, trenching is not applicable in this case.

Mechanical supports present devices that can be installed remotely, thus, making this method acceptable for deep water. A two-legged support is a device that changes the pipeline profile by means of lowering over a pipeline span and clamping to the pipe. It elevates the pipe and thereby reduces the curvature.

5.2.2 Rock Dumping

Rock dumping is a commonly used method for span mitigation. It is used both for changing the seabed profile before pipeline laying and correction of existing free spans after pipeline laying.

There are three main rock dumping techniques (Figure 5.4):

- Side dumping;

- Fall pipe;

- Bottom dropping.
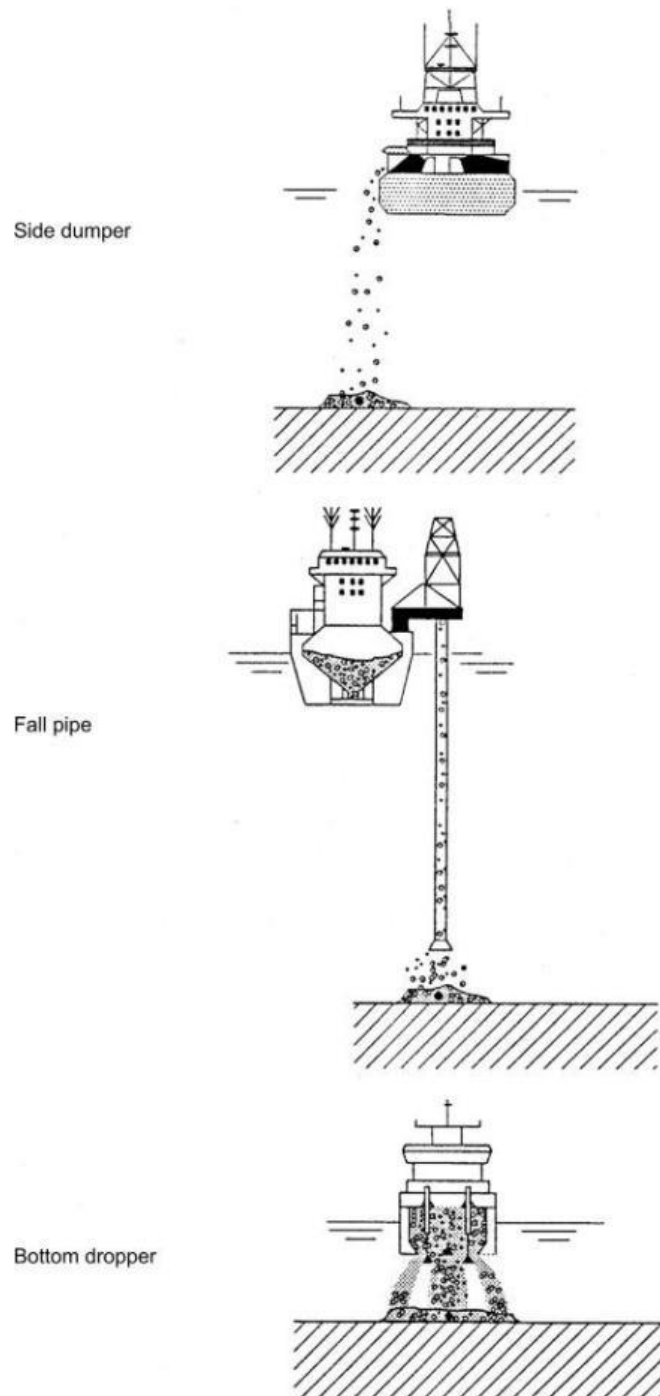
Figure 5.4 Methods of rock dumping (Bai and Bai, 2014)

Side dumping is based dropping the rock from the vessel board that is beforehand positioned over the necessary location. This method is efficient for local objects as it is necessary to dump a large quantity of rock for sustainable protection. In the case of pipeline protection, it is considered to be economically inefficient.

Fall pipe involves dropping the rock through a special tube form the vessel and moreover, this method implements a remotely operated vehicle (ROV) in order

to provide accurate dumping. Fall pipe method is suitable for pipelines and flowlines dumping as it minimizes the rock quantity and provide an accurate position.

Bottom dropping method is similar to the side dumping as it involves dropping a large quantity of the rock with low accuracy. Bottom dropping can be executed by means of either special barges which drop all the rock at once or ports that are opened at the bottom of the hold.

5.3 Environmental Assessment

Due to various external and internal factors, the probability of failure of a subsea pipeline is increasing that could lead to spills of oil and gas. A leakage of oil and gas causes dangerous accidents for human safety and environment. The risk of a subsea pipeline failure can not be eliminated totally, but mitigating measures should be analyzed and taken in order to reduce the probability of a leakage accident. The allocation of failure mechanisms for a subsea pipeline is shown in Table 5.1, according to Li et al. (2016).

Table 5.1 Allocation of failure mechanisms for subsea pipelines (Li et al., 2016)

Failure mechanism	Distribution
Corrosion	36%
Material	13%
External loads causing damage	38%
Construction damage	2%
Other	11%

According to DNVGL-RP-F107 (2017), material damage of a pipeline is classified as:

- Minor damage. Both repairing is not required and there is no release of hydrocarbons;
- Moderate damage. Damage requiring repair, but there is no release of hydrocarbons;

70

- Major damage. Damage leading to release of hydrocarbons.

Any damage leading to the hydrocarbon release may cause hazardous consequences for eco-system in the water, coastal environment, seabirds and fish in fish farms. The environmental impact is dependent on the amount of spillage, the weather conditions and time to reach the sensitive areas. A spillage is classified by DNVGL-RP-F107 (2017) and is shown in Table 5.2.

Table 5.2 Classification of spillages (DNVGL-RP-F107, 2017)

Category	Description	Amount of release
1 (low)	Insignificant on the environment.	~0
2	Minor release of pollution media. The release media will be neutralized by air or seawater.	<1000 tons
3 (medium)	Moderate release of polluting media. The release media will take some time to be neutralized by air or seawater.	<10000 tons
4	Large release of polluting media that can be removed.	<100000 tons
5 (high)	Large release of high polluting media that can not be removed.	>100000 tons

In the case of a concept of a pipeline protection connected with trenching and burial of the pipeline for shallow depth and rock dumping for deep water, there are some aspects in order to decrease the environmental impact:

- While burying a pipeline consider the safety factor k for determination the burial depth $d = k(1.96 + D_{pipe})$;
- Use small stones for pipeline dumping in order there is no spread of sand or other protection material;
- Minimize anchoring when putting protection in pace for minimizing the disruption of the seabed;
- Minimize use of heavy fuel for dumping vessels.

6 CONCLUSIONS

In this thesis, the behavior of ice ridges on the northeastern coast of Sakhalin island is investigated by means of implementation of two different methods, moreover, the behavior of the vortex-induced vibrations of two circular cylinders in three various configurations (L=4D;5D;6D) in a proximity of a plane wall is investigated by means of using CFD package OpenFOAM in upper transition regime ($Re = 3.6 \times 10^6$).

Based on the present research, the following conclusions can be formed:

- Two theoretical approaches, based on the force equilibrium and energy transfer, are investigated for the ice gouging calculations. Comparing these models, the energy model is considered to be more reliable providing realistic and consistent results;

- The gouge depth has been calculated and accounts for 1.96 m;

- The wall proximity magnifies the mean lift force, while the mean drag force remains approximately with the same value;

- The vorticities from the bottom surface disturb the symmetry in the wake of a cylinder, therefore, the oscillation frequency in the in-line direction is reduced by half. This factor is the reason of the resonance of both streamwise and transverse oscillation frequencies;

- As the distance between the cylinders decreases, the vortex shedding of the first cylinder induces the deviation of the trajectory of the second cylinder from its normal shape;

- The drag force is less in the second cylinder, as the vortex shedding causes the shielding effect: the flow velocity decreases due to the interaction with the first cylinder and, moreover, the vorticities of the first cylinder create lower pressure in the wake instigating the decreasing the value of the drag force of the second cylinder;

- Analyzing the protection methods of a pipeline, the efficient concept is to trench the pipe for $l = 170.9\,m, d = k\left(1.96 + D_{pipe}\right)$ and to dump the pipeline in deep water with the rock using fall pipe method in order to eliminate free spans and VIV phenomenon;
- In order to decrease the harmful impact on the environment, small stones should be used for pipeline dumping, it should minimize anchoring when putting protection in pace for minimizing the disruption of the seabed and it should minimize use of heavy fuel for dumping vessels.

6.1 Future Work

The current thesis has a big potential for the future investigation and implementation.

There are possible ideas for the future work:

- Simulate ice scouring model and calculate the gouge depth using CFD modelling.
- Study the ice-soil-pipe interaction at different burial depth of a pipe.
- Study on near-wall VIV of two cylinders at a range of reduced velocities U_r=5;6;7, which results show the dependence of response amplitude of each cylinder in lock-in zone.
- Study of different gap ratios. In this thesis the limiting gap ratio is equal to two, but using the overset mesh approach it is possible to setup cylinders closer to the bottom, which model is closer to reality.
- Study on 3D model of near-wall VIV of a single cylinder with anchoring one of its end and investigate the vortex shedding distribution.

REFERENCES

[1]   Bai, Q. and Bai, Y., 2014, Subsea pipeline design, analysis and installation, Elsevier Science & Technology.

[2]   Barrette, P., 2011, Offshore pipeline protection against seabed gouging by ice: An overview, Cold Regions Science and Technology, Vol. 69, 3-20.

[3]   Beaman, P. W., Zdravkovich, M. M., 1978, Flow around a circular cylinder near a plane boundary, Journal of Fluid Mechanics, Vol. 89, 33-47.

[4]   Beaman, P., 2011, Circular cylinder wakes and vortex-induced vibrations, Journal of Fluids and Structures, Vol. 27, 648-658.

[5]   Catalano, P., Wang, M., Iaccarino, G., Moin, P., 2003, Numerical simulation of the flow around a circular cylinder at high Reynolds numbers, International Journal of Heat and Fluid Flow, Vol. 24, 463-469.

[6]   Choi, K. and Lee, J.H., 2002, Simplified Ice Ridge-Seabed Interaction Model for Determination of Ice Scour Depth, Proceedings of The Twelfth International Offshore and Polar Engineering Conference, Kitakyushu, Japan, May 26-31.

[7]   DNVGL-RP-F107, 2017, Risk assessment of pipeline protection, Germanischer Lloyd, Hamburg

[8]   Duplenskiy, S.V., 2012, Protection of Subsea Pipelines against Ice Ridge Gouging in Conditions of Substantial Surface Ice, Master thesis, University of Stavanger, Norway.

[9]   Ferziger, J. H. and Perić, M., 2002, Computational Methods for Fluid Dynamics (third edition), Springer-Verlag.

[10]   Gudmestad, O. T., Zolotukhin, A. B., Ermakov, Jakobsen, R. A., Michtchenko, I. T., Vovk, V. S., Løset, S. and Shkhinek, K. N., 1999, Basics of Offshore Petroleum Engineering and Development of Marine Facilities with Emphasis on the Arctic Offshore, Oil and gas, Moscow.

[11]   http://pacificinfo.ru/data/cdrom/2/HTML/3_00.htm

[12]   http://www.ae.metu.edu.tr/tuncer/ae546/prj/delaundo/

[13]   http://www.cdu.ru/tek_russia/issue/2014/8/302/

[14]   https://skr.su/news/post/95615

[15]   ISO/FDIS 19906:2019(E), 2019, Petroleum and natural gas industries – Arctic offshore structures, ISO Geneva, Switzerland.

[16]   Janocha, M. J., 2018, CFD Simulations of Vortex-Induced Vibrations of a Subsea Pipeline Near a Horizontal Plane Wall, Master thesis, University of Stavanger, Norway.

[17]   Li, X., Chen, G. and Zhu, H., 2016, Quantitative risk analysis on leakage failure of submarine oil and gas pipelines using Bayesian network, Process Safety and Environmental Protection, Vol. 103, 163-173.

[18]   Li, Z., Prsic, M. A., Ong, M. C., Khoo, B. C., 2017, Large Eddy Simulations of Flow Around Two Circular Cylinders in Tandem in the Vicinity of a Plane Wall at Small Gap Ratios, Elsevier Science.

[19]   Li, Z., Yao, W., Yang, K., Jaiman, R. K., Khoo, B. C., 2016, On the vortex-induced oscillations of a freely vibrating cylinder on the vicinity

[20]   Menter, F. R., 1994, Two-Equation Eddy-Viscosity Turbulence Models for Engineering Applications, AIAA Journal, Vol. 32, No. 8.

[21]   Obert, K.M. and Brown, T.G., 2011, Ice ridge keel characteristics and distribution on the Northumberland Strait, Cold Regions Science and Technology, Vol. 66, No. 2.

[22]   Ong, M. C., Utnes, T., Holmedal, L. E., Myrhaug, D., Pettersen, B., 2010, Numerical simulation of flow around a circular cylinder close to a flat seabed at high Reynolds numbers using a $k-\epsilon$ _model, Coastal Engineering, Vol. 57, 931-947.

[23]   Ong, M. C., Utnes, T., Holmedal, L. E., Myrhaug, D., Pettersen, B., 2008, Numerical simulation of flow around a smooth circular cylinder at very high Reynolds numbers, Marine Structures, Vol. 22, 142-153.

[24]   Paulin, M., Cocker, J., Humby, D. and Lanan, G., 2014, Trenching of Pipelines for Protection in Ice Environments, OTC Arctic Technology Conference, Houston, Texas, February 10-12.

[25] Sarpkaya, T., 2010, Wave forces on offshore structures, Cambridge University Press.

[26] Shevchenko, G. V. and Tambovsky, V. S., 2018, Динамика дрейфа льда на северо-восточном шельфе острова Сахалин по данным измерений радиолокационными станциями, Южно-Сахалинск / The ice drift dynamics on the northeastern Sakhalin shelf from the measurements by radar stations, FASO Russia, Institute of marine geology and geophysics, Far Eastern branch of the Russian academy of sciences, Yuzhno-Sakhalinsk.

[27] Sumer, B.M. and Fredsøe, J., 2006, Hydrodynamic around cylindrical structures (Advanced Series on Ocean Engineering), World Scientific, Vol. 26.

[28] Vershinin, S.A., Truskov, P.A. and Liferov, P.A., 2008, Ice Action on Seabed and Subsea Structures, Russkaya kniga.

[29] Versteeg, H. K., Malalasekera, W., 2007, An introduction to Computational Fluid Dynamics: The Finite Volume Method (Second Edition), Pearson Education Limited.

[30] Walle, T., 2004, Ice Gouging offshore Sakhalin Island, Master thesis, University of Stavanger, Norway.

[31] Wilcox, D. C., 2010, Turbulence Modeling for CFD, DCW Industries.

[32] Williamson, C. H. K., Govardhan, R., 2004, Vortex-Induced Vibrations, Annual Review of Fluid Mechanics, Vol. 36, 413-455.

[33] Williamson, C. H. K., Govardhan, R., 2008, A brief review of recent results in vortex-induced vibrations, Journal of Wind Engineering and Industrial Aerodynamics, Vol. 96, 713-735.

[34] Yu, V., 2018, CFD Simulations of Near-wall Vortex-Induced Vibrations of Two Pipelines at High Reynold Number, Course work in Course Marine Operations, University of Stavanger, Norway.

APPENDIX A

```matlab
clc;
clear all;
close all;
```

Initial parameters

```matlab
% ice data
h=1.6; %Level ice thickness
hs=4; %Ridge sail height
hc=6; %Consolidated layer thickness
keelAng=30*pi/180; %Keel angle
sailAng=20*pi/180; %Sail angle
B=20; %Keel breadth
Tb=0.4; %Ridge block size
pIce=916; %Ice density
uIce=1.1;%ice speed
E=8; %Elasticity modulus
v=0.34; %Poisson's ratio
IceIntFricAng=20*pi/180; %Internal friction angle
porSail= 0.07; %Sail porosity

% Soil data
wallFricAng=25*pi/180; %Wall friction angle
intFricAng=30*pi/180;%Internal friction angle
iceSoilFric=0.5; %Friction between ice and soil
pSoil=1500; %Soil density
seaSlope=1*pi/180; %Seabed slope

% Environmental data
pWat=1030; %Water density
uCur=3.6; %Current speed
Cdc=0.9; %Current drag coefficient
pAir=1.3; %Air density
uAir=30; %Wind speed
Cdw=0.9; %Wind drag coefficient
skinWind=0.001; %wind skin coefficient

g=9.81;

macPor=0.11*log(Tb)+0.37; %Ridge macro porosity
prw=macPor*pWat+(1-macPor)*pIce; %Ridge density in water
pra=porSail*pAir+(1-porSail)*pIce; %Ridge density in air

hk=3.95*hs; %Keel draught
bw=3.91*hk; %Keel width at the water line
bk=bw-2*hk*cot(keelAng); %Keel width at the bottom
Ac=(hk-pIce/pWat*h)*B; %Current projected area
Aw1=(hs-(pWat-pIce)/pWat*h)*B; %Wind projected area
Aw2=bw*B; %Wind projected area (skin effect)
```

APPENDIX A

Force model

```
syms d;

Fdw=0.5*pAir*Cdw*Aw1*uAir^2+0.5*skinWind*pAir*Aw2*uAir^2;
Fdc=0.5*Cdc*pWat*Ac*uCur^2;

Fb=pWat*g*B*(0.5*(bw+bk)*(hk-pIce/pWat*hc)+pAir/pWat*hc*bw);
Ff=0.43*4.059*B^0.622*h^0.628;

Kp=(cos(intFricAng))^2/cos(wallFricAng)/(1-
(sin(intFricAng+wallFricAng)*sin(intFricAng)/cos(wallFricAng))^0.5)^2;
Pf(d)=0.5*Kp*pSoil*g*(d+0.635*d)^2*B;
Ps(d)=1/6*Kp*pSoil*g*d^2*bk*(bk+d*cot(keelAng)/2);

Fcx(d)=iceSoilFric*Pf(d)*cos(wallFricAng)*cos(keelAng)+iceSoilFric*Ps(d)*cos(
wallFricAng);

Ffr(d)=iceSoilFric*iceSoilFric*Pf(d)*cos(wallFricAng)*sin(keelAng);

eqn1=Fdw+Fdc+Ff*10^6-Ffr(d)-Fcx(d)==0;

slv1=solve(eqn1,d);

root1=vpa(slv1);
depth1=root1(root1>0);

display(depth1);
```

```
depth1 = 2.5757865928632676756708637863869
```

APPENDIX A

Energy model

```
syms l y x;

W=prw*B*g*(pra/prw*(hs-(pWat-
pIce)/pWat*hc)^2*cot(keelAng)+pIce/prw*hc*bw+0.5*(bw+bk)*(hk-pIce/pWat*hc));

Ek=W*uIce^2/2/g;

Wc(l)=int(0.5*Cdc*pWat*Ac*(uCur-(l-x)/l*uIce),x,0,l);
Ww(l)=int(0.5*pAir*Cdw*Aw1*(uAir-(l-x)/l*uIce)^2+0.5*skinWind*pAir*Aw2*(uAir-(l-
x)/l*uIce)^2,x,0,l);
Wf(l)=int(x/l*0.43*4.059*B^0.622*h^0.628*10^6,x,0,l);

C1=cot(keelAng)/(1-cot(keelAng)*tan(seaSlope));

xx(y)=1000/17*y+10000/289*10^0.5*y^0.5;
yy(x)=500/289+17/1000*x-1/289*(250000+4913*x)^0.5;

Pf1(x)=0.5*Kp*pSoil*g*((1.691*(x*tan(seaSlope)-yy(x)))*(1+C1*tan(seaSlope)))^2*B;
Pf2(y)=0.5*Kp*pSoil*g*((1.691*(xx(y)*tan(seaSlope)-y))*(1+C1*tan(seaSlope)))^2*B;

Ps(x)=1/6*Kp*pSoil*g*cot(seaSlope)*(x*tan(seaSlope)-yy(x))^3;

Wcx(l)=int(iceSoilFric*Pf1(x)*cos(wallFricAng)*cos(keelAng)+iceSoilFric*Ps(x)*cos(wall
FricAng),x,0,l);
Wcy(l)=int(iceSoilFric*Pf2(y)*cos(wallFricAng)*sin(keelAng),y,0,yy(l));

Ep(l)=pWat*g*B*bw*(yy(l))^2/2;

ki=(E*10^9*h^3*pWat*g/24/(1-v^2))^0.5;

Ei(l)=ki*(yy(l))^2/2;

Wfr(l)=int(iceSoilFric*(pWat*g*B*bw*yy(x)+ki*yy(x)+iceSoilFric*Pf1(x)*cos(wallFricAng)
*sin(keelAng)),x,0,l);

eqn2=Ek+Ww(l)+Wc(l)+Wf(l)==Wfr(l)+Wcx(l)+Wcy(l)+Ep(l)+Ei(l);

slv2=solve(eqn2,l);
root2=vpa(slv2);

length=root2(root2>0);
deproot=length*tan(seaSlope)-yy(length);
depth2=vpa(deproot);
display(length);
display(depth2);
```

```
length = 170.87967219805419862437394478176
depth2 = 1.9594443852774734334217878522684
```